Università degli Studi di Padova

Facoltà di Ingegneria

Tesi di laurea

Characterization of a grazing incidence spectra-imager laboratory model for solar observation

Relatore: Dott. Luca Poletto

Correlatore: Dott. Fabio Frassetto

Laureando: Paolo Miotti

Corso di laurea in INGEGNERIA ELETTRONICA

December 5, 2011

Abstract

This thesis describes the work made on the optical characterization of a laboratory demo-model stigmatic grazing-incidence spectra-imager for solar investigation. This instrument, stigmatic in an extended field of view, can acquire spectral features between 4 nm and 20 nm, even preserving spatial information. The system consists of a double telescope in the KirkPatrick-Baez configuration and a grazing incidence spectrograph.

Contents

Introduction

The understanding of the nature of the solar atmosphere have wide-reaching applications. Some questions have relevance to all the stars and to an understanding of the solar-terrestrial system, since Earth's environment is influenced by solar radiation and ejecta. Like all the atmospheres, the Sun's has a temperature and density profile. The level that we see in visible wavelengths, we call the photosphere, is the effective apparent surface of the Sun. The temperature of the photosphere's plasma is about 6000 K. The density of the plasma decreases rapidly through the overlying chromosphere, whereas the temperature of it increases. Above the chromosphere is the corona, where temperatures rapidly climb to more than 10 million K and there is an additional reduction of density of the plasma. In Fig. 1 the temperature profile of the solar atmosphere is showed. The determination of the plasma characteristics (densities, temperatures, flow velocities, abundance etc..) with appropriate temporal, spatial and spectral resolutions is then fundamental for the study of the structure and the evolution of the solar atmosphere.

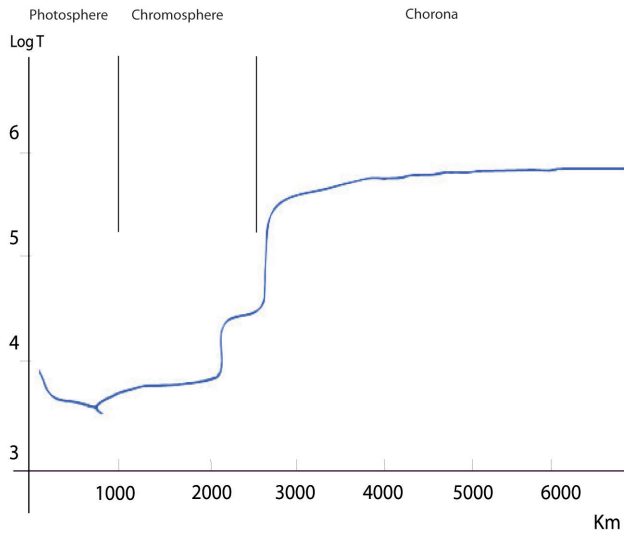

Figure 1: Solar atmosphere's temperature profile.

If we consider some existent instruments employed for this purpose, we can note how much important results have been taken in this way. For example, in the SOHO (SOlar and Heliospheric Observatory) satellite, launched in 1995, a grazing-incidence telescope-spectrograph, CDS (Coronal Diagnostics Spectrometer) and a normal-incidence spectrometer, UVCS (UltraViolet Coronograph Spectrometer), have been applied to perform spectra imaging of the Sun's corona. SUMER (Solar Ultraviolet Mesurements of Emitted Radiation), a normal incidence spectra-imager, has been applied to observe the the solar atmosphere, from the chromosphere to the inner corona. It is worth to be noted that all these instruments weren't designed for the soft X-ray (see Appendix A.1) spectrum of the solar atmosphere [1].

The lattest soft X-ray analysis of the solar atmosphere was conducted in the SMM (Solar Maximum Mission) with a high resolution rocket-borne grazing-incidence spectrograph on 1982, but the temporal resolution requirements for a dynamic study of the solar atmosphere were not performed by the instrument [2].

Here we are presenting a new concept of high resolution spectra imager for the solar disk that operates at grazing incidence (see Appendix A.3) and is stigmatic in a large field of view. It is designed to acquire information through the study of solar plasma's emission line in the extreme ultraviolet (XUV) and soft X-Ray regions of electromagnetic spectrum. These regions are particulary important for the detection of emissions from the hottest plasmas of the solar atmosphere.

A spectrograph, even in the ideal aberration free case (see Appendix A.2), has intrinsic spatial-resolution capability only in the plane perpendicular to the spectral dispersion plane: the spatial distribution of an extended source can be analyzed only in the direction parallel to the entrance slit. In the case of a so called astigmatic configuration, only spectral aberrations are corrected by the optical design, so a pointlike source placed on the entrance-slit plane and on the optical axis is imaged on the focal plane on a narrow line almost parallel to the slit itself (see Fig.2 a)). Such a configuration is not able to provide simultaneous observations of extended regions, which is an important task for solar physics: images of the Sun's disk or of the solar corona can be built by means of scanning over the whole region to be observed, point by point. Conseguently, long acquisition time to acquire a complete image and complex scanning mechanisms are required.

In a so-called stigmatic spectrograph, the aberrations are corrected both on the spectral dispersion plane and on the plane perpendicular to this, so a pointlike source placed on the entrance-slit plane and on the optical axis is imaged as a point on the focal plane (see Fig. 2 b)). If the stigmatic behaviour is maintained in a sufficiently large field of view, it is possible to obtain images of extended regions by moving the spectrograph only in the direction perpendicular to the slit; this simplifies the mechanical complexity and minimizes the image-acquisition time.

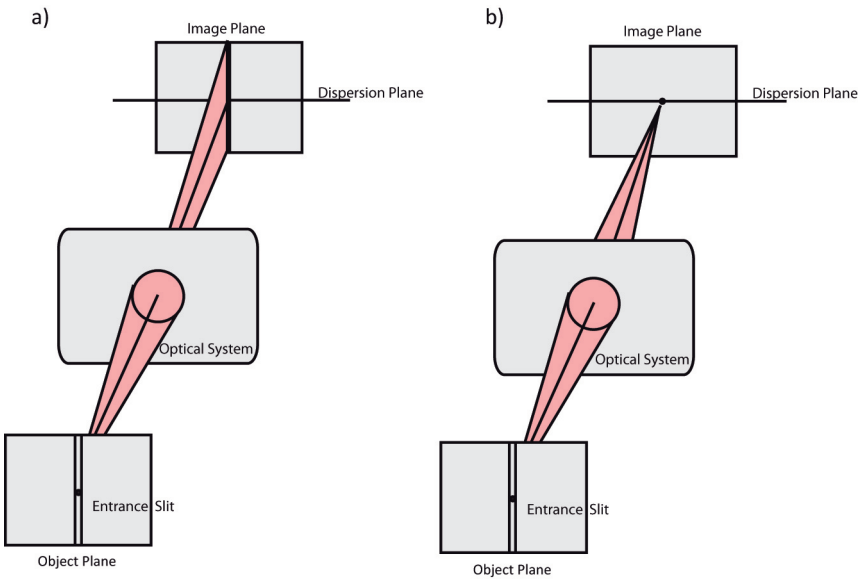

Figure 2: Astigmatic a) and stigmatic b) optical systems.

Whereas normal-incidence stigmatic spectrographs with toroidal classical grating (see Appendix A.5), have been successfully used for diagnostics of extended sources in both laboratory and space applications, in grazing-incidence functioning it is almost impossible to correct the astigmatism with this optics in an extended spectral region [3]. At this title, UVCS and SUMER (normal incidence spectrographs with toroidals classical gratings) provides a stigmatic imaging employing a slit, while CDS cannot provides stigmatic imaging because it is used in grazing incidence and thus, the use of a pinhole is required for this instrument [1]. An almost flat focal surface, but again affected by astigmatism, at near-normal incidence on the detector is instead obtained by using spherical variable-line-spaced gratings (see Appendix A.5). In such a system the aberrations can be controlled by the ruling parameters for groove-space variation. When we choose a proper line-spacing distribution, the spectral focal curve can be brought to be the closest to the detector plane. Stigmatic designs proposed up to now in the latter case use a SVLS grating coupled with a toroidal mirror with the tangential focusing point on the entrance slit of the spectrograph and the sagittal focusing point on the focal plane. The image of an on-axis emitting point is finally stigmatic, but it broadens in both directions for off-axis points, so both spectral and spatial resolutions decrease far from the optical axis. The instrument here analyzed just trace this kind of design with some improvements.

The optical design is compounded by two telescopes and a spectrograph: Telescope I consists of a single cylindrical mirror with parabolic section, focusing the radiation on the entrance slit of the spectrograph in the spectral dispersion plane; Telescope II consists of two cylindrical mirrors with aspherical section in a Wolter II configuration (see Appendix A.4.2), focusing the radiation on the spectrograph focal plane in the spatial plane. Telescope I and telescope II are mounted in a Kirkpatrick-Baez Configuration (see Appendix A.4.1). The spectrograph consists of a grazing-incidence spherical variable-line-spaced grating with flat-field properties. Telescope II is mounted with its tangential plane coincident with the grating equatorial plane. The spectrum is acquired by a detector mounted at near-normal incidence with respect to the direction of the exit beam. This unique configuration provides focal images of extended sources with negligible spectral broadening even far from the optical axis and a spatial broadening depending only on the performance of telescope II. A relatively large field of view is obtained in the direction parallel to the slit with constant spectral resolution and slightly degrading spatial resolution. Images of extended regions are then obtained by means of moving the instrument only in the direction perpendicular to the slit. The instrument works in the region from 4 nm to 20 nm, with a spectral resolution of 0.1 % at 10 nm and a spatial resolution of 3.5 arcsec over a field-of-view of 0.5 degrees (approximately the extension of the solar disk seen from the Earth), within a total envelope of 1.3 m. A Schematic view of the instrument in the spectral plane and in the spatial plane is presented in Fig. 3.

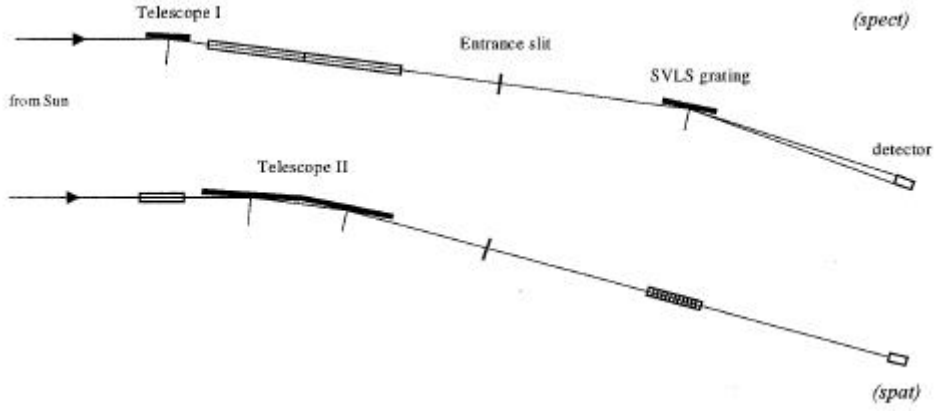

Figure 3: Schematic view of the instrument in the spectral plane and in the spatial plane.

The main goal of this work of thesis is to acquire specifics information that could allow us to conclude that the imaging properties of the instrument are in agreement with simulations. These simulations have been made with ZEMAX ray-tracer simulator. The use of ray-tracing techniques can provide a general method for evaluating complex systems in full detail.

Chapter 1

A similar instrument: CDS

1.1 Choronal Diagnostic Spectrometer

Due to his structure, very similar on our instrument, it results particulary instructive a detailed describtion of this spectrometer. The optical elements of CDS are shown in Fig.1.1; A grazing incidence Wolter-Schwartzchild type 2 telescope feeds simoultaneously a normal incidence spectrometer and a grazing incidence spectrometer which share a common slit.

As indicated by the light stop in Fig 1.1, between the telescope and the slit assembly, two portion of the telescope are selected, one for each spectrometer. In the normal incidence spectrometer, after a single normal incidence reflection of two toroidal gratings, the in-coming beam is focused onto an intensified CCD detector, producing two spectrally dispersed stigmatic images. To build up larger images a plane mirror in front of the slit is scanned through a small angle in 2 arcsecond steps.

The grazing incidence spectrometer instrument adopts a classical Rowland configuration with a classical spherical uniform-line-spaced grating. In the classical Rowland configurations the entrance slit, the grating and the detector are placed on a circle with diameter equal to the radius of the grating (see Fig. 1.2). The spectrum is acquired by a detector mounted tangent to this circle, so the length of the exit arm changes as the cosine of the diffraction angle; It is impossible to correct the astigmatism with a fixed mirror in an extended spectral region because of this rapid variation; the variable exit arm gives large defocusing far from the stigmatic wavelength [4]. Conseguently, images are built to scan over the solar surface point by point. Four microchannel plate detectors are placed around the Rowland circle; the resulting spectra are obviously astigmatic. Thus, for grazing incidence operation, pin-hole slits are used. This limitations is due to the lack of spectroscopic grazing-incidence stigmatic configurations when the SOHO instrumentation was conceived [1].

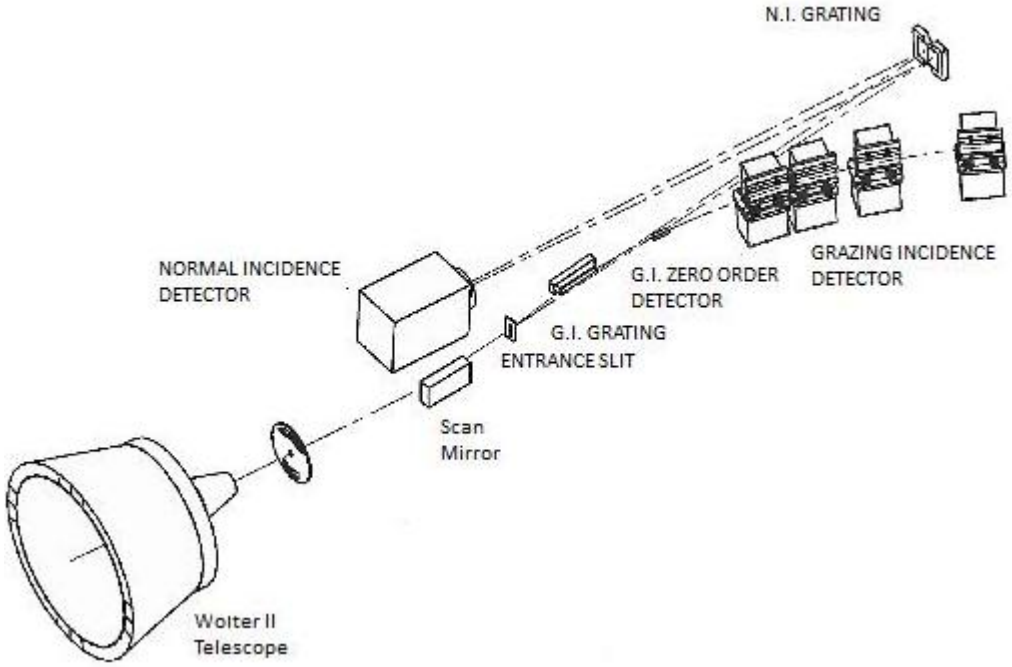

Figure 1.1: CDS Optical Layout. The normal incidence and the grazing incidence sections of the spectrometer are visible.

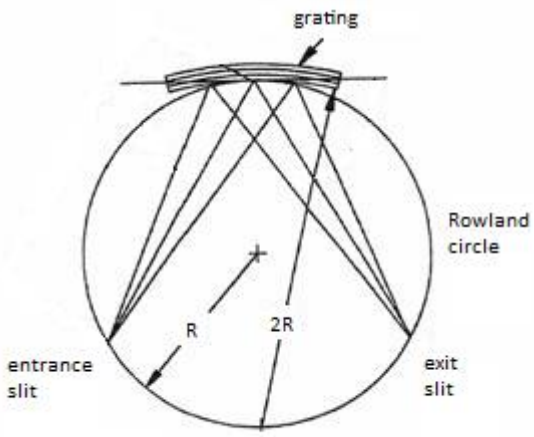

Figure 1.2: Rowland circle. The entrance slit, the grating and the detector are placed on a circle with diameter equal to the radius of the grating.

To enable images to be built up the slits can be move in one arcsecond increments in a plan perpendicular to the direction of the dispersion while the scan mirror can be moved in two arcsecond increments in the plane of dispersion. The field of wiev of the telescope is 4 arcminutes. To cover the whole solar disk the instrument can be repointed through an angle of $\pm 0.75°$.

Analyzing the performance of past EUV space borne instrumentation, it becomes clear that CDS experiment represents the first thorough examination of the EUV region of the Sun. EUV detectors have been directed at the Sun since OSO I in 1962, but if our demands are wavelength coverage extending to the 15-40 nm region, in order to include the emission of the hottest coronal plasmas, some spatial resolution and some spectral resolution, only four experiments are found to satisfy these demands. These are the EUV OSO VII Experiment (1972), the slitless spectrograph on SkyLab (1973-1974) the CHASE (Choronal Helium Abundance Experiment) on SpaceLab II (1985) and the SERTS (Solar EUV Rocket Telescope and Spectrometer) rocket experiment. Altough the SkyLab slitless spectrograph covered the wavelength range from 17,1 to 63 nm, it could not be used to unambiguously separate spectral and spatial information. Also, it was photographic which provided a very restricted temporal resolution. The CHASE and the SERTS instruments flew on the Shuttle and on a rocket series respectively and were thus of short duration. In addition, the SERTS flights to date used film, again, limiting the temporal capabilities. Finally, the spatial resolution of the OSO VII experiment was of order 20 arcseconds, some 7 times coarser than that of CDS. It is clear that CDS is a unique device, ideal for tackling the coronal goals of SOHO [1].

Some general characteristics of CDS and its performance are summarized in table 1.

Table 1: General characteristics of CDS

General		
	Total Mass	100 Kg
	Overall length	1,7 m
	Average Power	58 W
	Telemetry rate	11,3 Kbit/s
Telescope		
	Outer f/#	9,38
	Eff. focal length	257,831 cm
	FWHM	< 2 arcsec
	Full geometric area	289,28 cm^2
	Plate Scale at Slit	12,5 μm/arcsec
Mechanism details		
	Pointing	Anywhere on disk and low corona
	Raster step sizes	E-W= 2,032 arcsec N-S=1,016 arcsec
NIS		
	Telescope aperture used	34,3 cm^2 per grating
	Wavelength ranges	308-381, 513-633 $\mathring{A}$
	Prime slits	$2 \times 240{,}4 \times 240{,}9 \times 240$ arcsec
	Grating ruling	2400 and 4000 lines/mm
	Slit-Grating dist.	736,5 mm
	Grating-Detector dist.	744,6 mm
GIS		
	Telescope aperture used	47 cm^2 per grating
	Wavelength ranges	151-221, 256-338 393-493, 656-785 $\mathring{A}$
	Prime slits	$2 \times 2{,}4 \times 4{,}8 \times 50$ arcsec
	Grating ruling	1000 lines/mm
	Rowland circle radius	750 mm

Chapter 2

The instrument

2.1 Instrument overview

The instrument is opportunely mechanically designed, so all its components are located in an enclosed optical bench realized to work in vacuum; This also enables all the contamination sensitive component to be proctected, as well as allowing all the optical components to be maintained aligned. The chamber is kept at high vacuum using a couple of pumps. In Fig. 2.1 and in Fig. 2.2 is presented the instrument's optical bench; it is possible to note all the vacuum components used for our purpose.

The global telescope is divided into two sections: Telescope I consists of a single grazing-incidence mirror (see Appendix A.5) (cylindrical mirror with parabolic section) focusing the radiation on the entrance slit of the spectrograph (spectral slit) only in the spectral dispersion plane; Telescope II consists of two grazing-incidence mirrors (cylindrical mirrors with aspherical section in a Wolter II configuration) focusing the radiation on the spectrograph focal plane only in the direction perpendicular to the spectral dispersion plane. The spectrograph consists of a grazing-incidence SVLS grating with flat-field properties (see Appendix A.5). Finally, the spectrum is acquired by a detector mounted at near-normal incidence with respect to the direction of the exit beam: both microchannel-plate-based and EUV-enhanced CCD detectors can be used. Telescope II is crossed with respect to the grating and to telescope I; i.e., its mirrors are mounted with their tangential planes coincident with the grating equatorial plane. The spectral and the spatial focusing properties are then almost fully uncoupled: spectral aberrations on the focal plane are controlled only by the grating, whereas aberrations in the plane perpendicular to the dispersion plane are controlled only by the two mirrors of telescope II. The focal image of an extended source has a negligible spectral broadening even far from the optical axis and a spatial broadening depending only on the performance of telescope II. A relatively large field of view is obtained in the direction parallel

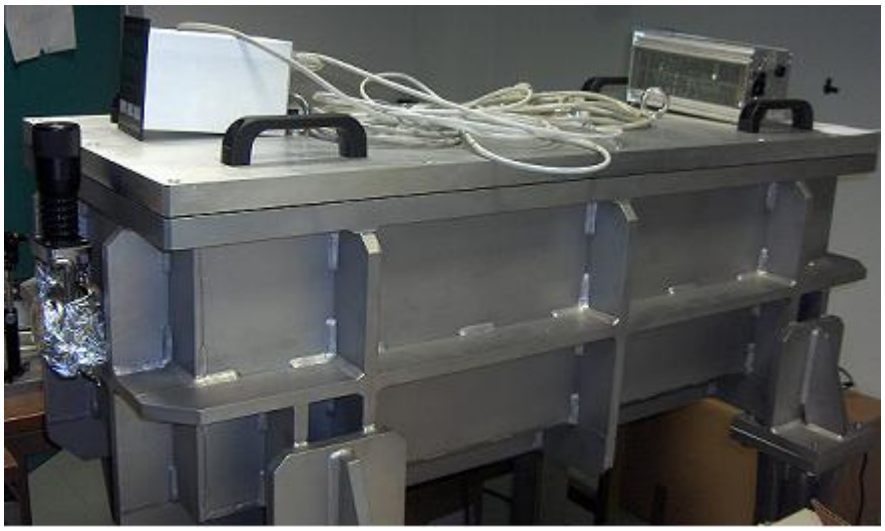

Figure 2.1: Instrument's optical bench, sect.1.

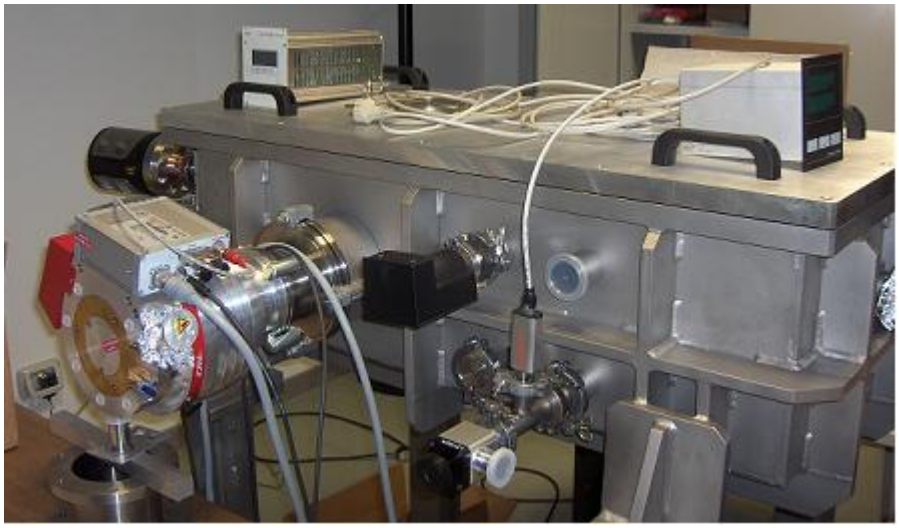

Figure 2.2: Instrument's optical bench, sect.2.

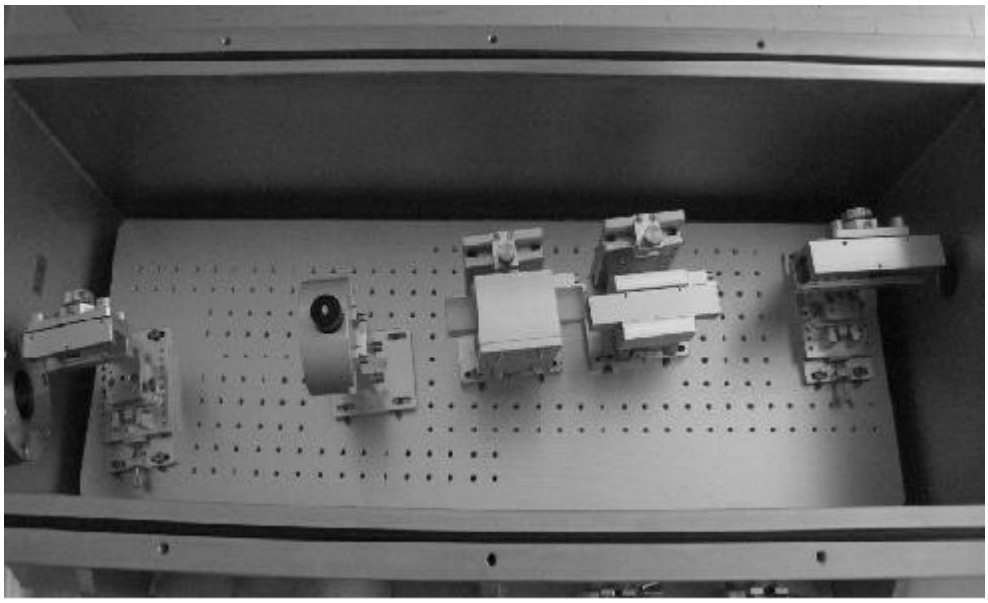

Figure 2.3: Instrument overview.

to the slit with constant spectral resolution and slightly degrading spatial resolution. Images of extended regions are then obtained by means of moving the instrument only in the direction perpendicular to the spectral slit [5].

An overview of the laboratory model is presented in Fig. 2.3. The optical layout of the instrument is presented in Fig. 2.4; both the spectral dispersion's plane and its perpendicular one are shown. The main instrumental parameters are summarized in Table 2.

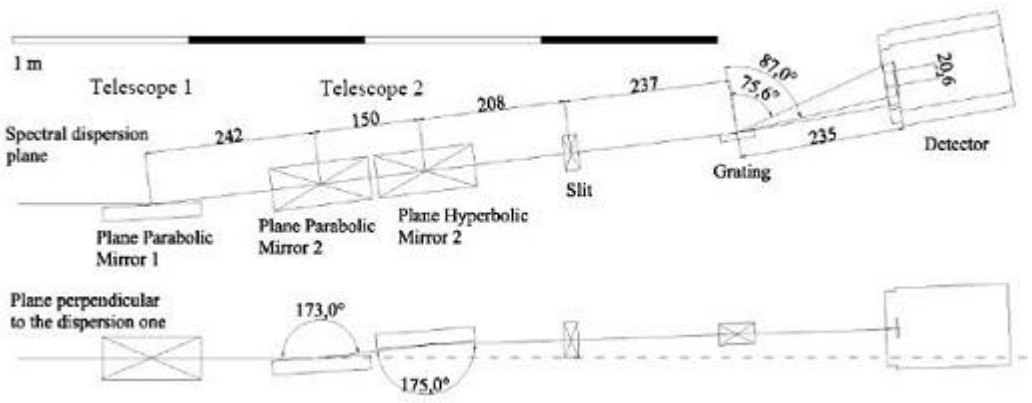

Figure 2.4: Optical layout of the instrument.

Table 2: Instrumental parameters.

General		
	Wavelength range	4-20 nm
	Field of view	± 0.25 °
Telescope I: Plane parabolic		
	Incidence angle	86,5 °
	Size	140 mm × 30 mm × 20 mm
	Clear aperture	130 mm × 10 mm
	Coating	40 nm Ni
	Focus to midpoint	600 mm
Telescope II: Wolter II plane parabolic + plane hyperbolic		
	Incidence angle	Par.:86,5 ° Hyp.:87,5 °
	Size	140mm × 30 mm × 20 mm
	Clear aperture	130 mm × 10 mm
	Coating	40 nm Ni
	Equivalent focal length	1204 mm
Spectrometer SVLS grating		
	Incidence angle	87 °
	Entrance arm	237 mm
	Exit arm	235 mm
	Radius	5649 mm
	Size	50 × 30 × 10 mm
	Central groove density	1200 gr./mm
	Parameters for	$d_0 = 1200$ mm$^-1$
	groove space	$d_1 = -8,497$ mm$^-2$
	variation	$d_2 = 5.1410^-2$ mm$^-3$
		$d_3 = -3,1510^-4$ mm$^-4$
	Profile	Saw tooth blazed @ 10 nm
	Coating	Gold
Detector CCD 16 bit		
	Pixel size	20 μm × 20 μm
	Active area	26,8 mm × 8 mm

2.2 The Telescope

The imaging capabilities are provided by a crossed telescope in the Kirkpatrick-Baez configuration (see Appendix A.4.1): the telescope I consists of a cylindrical mirror with parabolic section, focusing on the slit of the spectrograph in the spectral dispersion plane; the telescope II, schematized in Fig. 2.5, consists of two cylindrical mirrors with aspherical section in Wolter II configuration (see Appendix A.4.2), focusing on the focal plane in the direction perpendicular to the spectral dispersion. The telescope II is mounted with its tangential plane coincident with the equatorial plane of the telescope I. The spatial resolution in the direction perpendicular to the slit is given by the telescope I. The spatial resolution in the direction parallel to the slit, for the off-axis angles also, is instead given by the Wolter II-type telescope II.

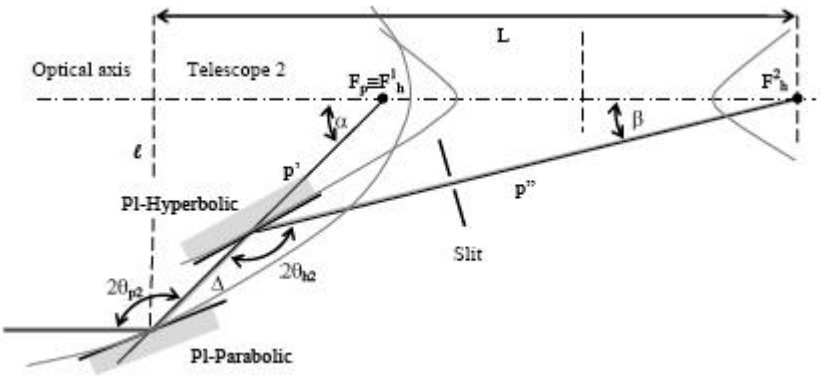

Figure 2.5: Details of Wolter II telescope.

The free parameters of the Wolter II configuration are: the incidence angle on the parabolic and hyperbolic mirrors θ_{p2}, θ_{h2}, the separation between these two optics Δ, and the exit arm p ". The connections between these four driving parameters and the other parameters of the telescope are provided by the equations 2.1-2.5. In these equations, α and β are the angles formed with the optical axis respectively by the central ray between the two mirrors and by the central ray on the focal plane. p ' is the virtual entrance arm of the hyperbolic mirror, f_p and f_h are the focal lengths respectively of the parabolic and hyperbolic mirrors. a and b are the hyperbolic parameters, l is the distance between the center of the first mirror and the optical axis, and L is the distance, measured along the optical axis, from the center of the first mirror to the focal plane.

$$\alpha = \pi - 2\theta_{p2}, \qquad \beta = 2\theta_{h2} - 2\theta_{p2}; \tag{2.1}$$

$$p' = p'' \frac{sin\beta}{sin\alpha}; \tag{2.2}$$

$$f_p = (p\,' + \Delta) cos^2\theta_{p2}, \qquad f_h = \frac{p\,'' cos\beta - p\,' cos\alpha}{2}; \tag{2.3}$$

$$a = \frac{p\,'' - p\,'}{2}, \qquad b = \sqrt{f_h^2 - a^2}; \tag{2.4}$$

$$l = (p\,' + \Delta) sin\alpha, \qquad L = p\,'' cos\beta + \Delta cos\alpha. \tag{2.5}$$

The effective focal length of the second telescope, f_{eff}, can be calculated considering an entrance ray forming an angle δ with the optical axis. Due to this inclination, the focal spot is translated by a quantity Δ on the focal plane, and f_{eff} can be calculated as:

$$f_{eff} = (p\,' + \Delta) \frac{[p\,'' + \Delta - \Delta \frac{sin(\frac{\pi}{2} - \theta_{h2})}{sin(\frac{\pi}{2} - \theta_{h2} - \delta)}]}{[p\,' + \Delta - \Delta \frac{sin(\frac{\pi}{2} - \theta_{h2})}{sin(\frac{\pi}{2} - \theta_{h2} - \delta)}]}. \tag{2.6}$$

In the case a small δ the equation can be simplified in:

$$f_{eff} = (p\,' + \Delta) \frac{p\,''}{p\,'}, \tag{2.7}$$

that in our case is about 1204 mm.

2.3 The spectrograph

The spectrograph is based on the use of a spherical variable-line-spaced grating (see Appendix A.5). The variation of the groove density along the direction perpendicular to the grating grooves is described as:

$$d(y) = d_0 + d_1 y + d_2 y^2 + d_3 y^3, \tag{2.8}$$

where d_0 is the central groove density, d_1, d_2, d_3, the ruling parameters, and they are optimized to respectively: make the focal curve as close as possible to the detector plane (in the spectral range of interest), minimize the coma, and minimize the spherical aberration (see Appendix A.2).

Chapter 3

Sources of radiation

Obviously, it is necessary to "simulate" Sun's light with well-collimated extended XUV and soft X-ray sources. The collimation is reached using a collimator located in a little chamber behind the instrument; Its duty is to make parallel the rays from the source. It is also clear that the instrument must be maintained in high vacuum, even when the source is changed or replaced. Operationally, it is important that the design of the source allows an expeditious change of the anode without breaking chamber vacuum and without disturbing the apparatus alignment and configuration. Additionally, it is necessary to maintain a high vacuum, comparable to the instrument's chamber in the vacuum chamber that contains the collimator and in the source. To reach this aim a valve gate is used to insulate the instrument chamber from the collimator and the source; so, vacuum in the instrument chamber can be manteined separeted from vacuum in the collimator and the source by using two couple of pumps (a couple for the instrument's chamber and a couple for the vacuum chamber and the source). A scheme of this configuration is reported in Fig. 3.1.

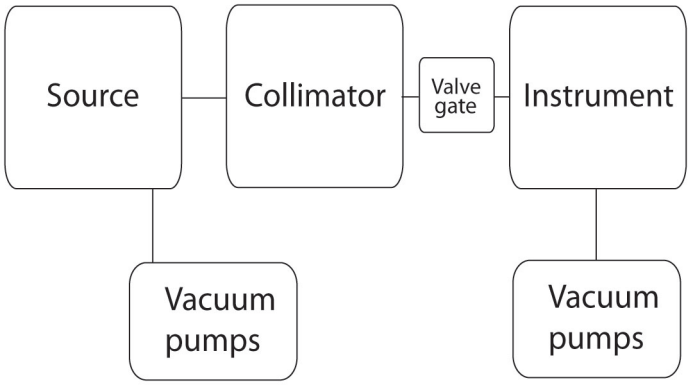

Figure 3.1: Configuration of the apparatus formed by the source, the collimator, the vacuum pumps and the instrument.

There are several mechanisms that brings to the emission of XUV and soft X-ray radiation. Natural proccesses are nearly always spontaneus and the emission is isotropic and globally non syinchronized (incoherent emission). These spontaneous procceses can even call down stimulated emission, so coherent XUV and soft X-ray radiations are emitted. The spontaneus emission can be realized in two different ways:

- **Bremsstrahlung:** This radiation is produced by the electrons as they are decelerated by the strong electric field near the high-Z (proton number) nuclei (see Fig. 3.3). The electron loses his kinetic energy, which is converted into a photon because energy is conserved. The resulting spectrum is characterized by a continuous distribution (see Fig. 3.2) which becomes more intense and shifts toward higher frequencies when the energy of the electrons is increased.

- **XUV and X-ray fluorescence:** If the electron has enough energy it can knock an orbital electron out of the inner electron shell of an atom, and as a result electrons from higher energy levels then fill up the vacancy and XUV and X-ray photons are emitted. This process produces an emission spectrum of XUV and X-rays at a few discrete frequencies (see Fig. 3.2), sometimes referred to as the spectral lines. The spectral lines generated depend on the target (anode) element used and thus are called characteristic lines. Usually these are transitions from upper shells of the atom into K shell (called K lines), into L shell (called L lines) and so on (see Fig. 3.4).

For our purpose we have used two different sources: a Manson X-ray source and a hollow-cathode XUV lamp.

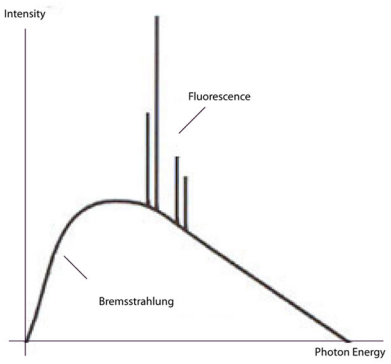

Figure 3.2: A typical soft X-ray spectrum. Bremsstrahlung and fluorescence are visible.

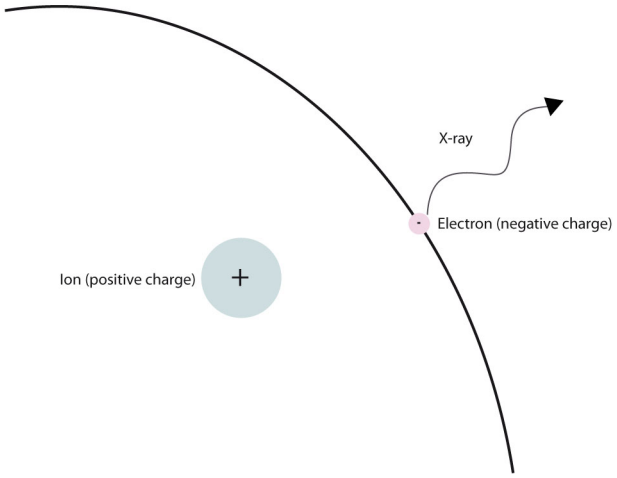

Figure 3.3: Bremsstrahlung. The electrons are scattered by the strong electric field near the high-Z nucleus and radiation is emitted.

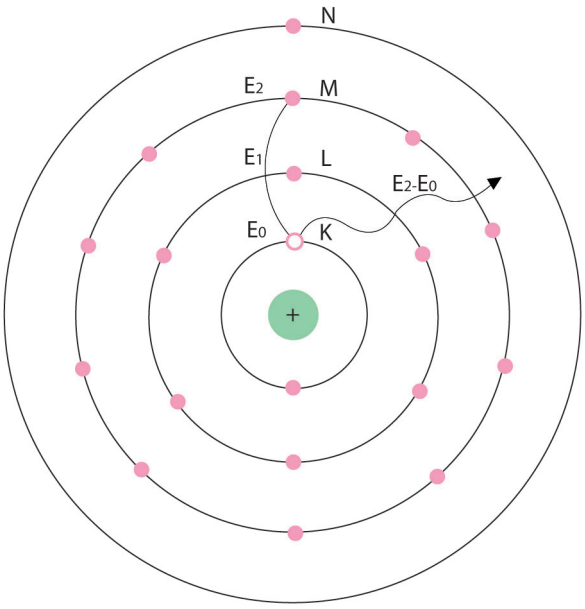

Figure 3.4: XUV and X-ray fluorescence. The electron has enough energy to knock an orbital electron out of the inner electron shell of an atom, as a result electrons from higher energy levels fill up the vacancy and XUV and X-ray photons are emitted.

3.1 The Manson X-ray source

The Manson source is an electron impact source. A tungsten filament is heated to produce electrons that are accelerated down a voltage gradient to impact a solid anode, usually made of carbon, copper, silicon, alluminium and magnesium (see Fig. 3.5). These electrons impact on the anode's atom exciting them; as these excited atoms decay to lower states, they will emit radiation. A power source is used to establish the currents and potentials needed to run the X-ray Manson source. In Fig. 3.6, the Manson source used for our purposes is showed. For our purpose, we will only use carbon, silicon and alluminium anodes. Some typical spectra, provided with different anodes, are shown in Fig. 3.7.

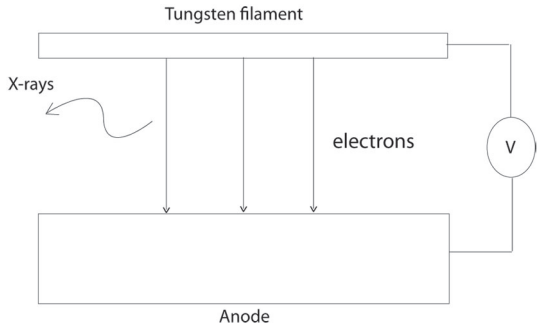

Figure 3.5: X-ray source scheme.

Figure 3.6: Manson source.

The design of the Manson source allows an expeditious change of the anode without breaking chamber vacuum and without disturbing the apparatus alignment and configuration. This characteristic, together with his stability and compactness, makes the Manson source a very useful instrument for the generation of soft X-ray radiation.

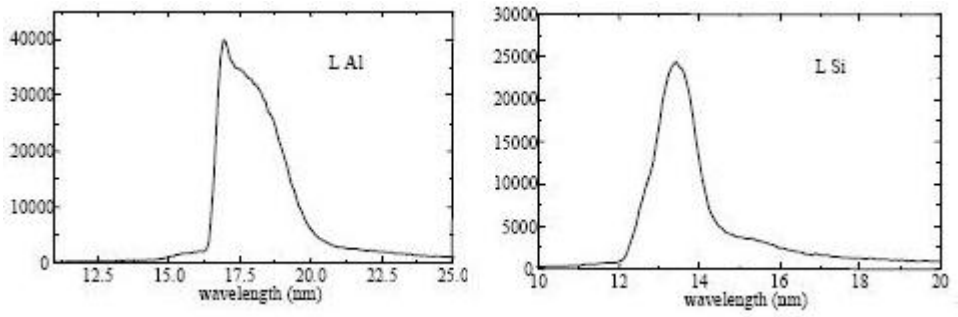

Figure 3.7: Typical Manson source's spectra. L-shell Alluminium and L-shell Silicon spectra are presented.

3.2 The hollow cathode XUV lamp

Hollow cathode lamps consist of a cathode, an anode, and an inert gas contained in a glass envelope (usually argon, neon, or helium). A high voltage (800-900 V) is applied across the anode and the cathode, resulting in an ionization of the filling gas. The gas ions will then be accelerated into the cathode, sputtering off atoms from the cathode. Both the buffer gas and the sputtered cathode atoms will in turn be excited by collisions with other atoms/particles in the plasma. As these excited atoms decay to lower states, they will emit radiation. Either the spectrum from the buffer gas or the sputtered cathode material itself, or both, may be of interest. The hollow cathode lamp used for our purposes is showed in Fig. 3.8. A power source is used to establish the currents and potentials needed to run the hollow cathode lamp source. A typical spectrum with a lamp filled with Helium is shown in Fig. 3.9 (only the region around 23-30 nm is rappresented). We can note that helium filled hollow cathode lamp present a narrower spectrum respect Manson source's spectra. Infact, hollow cathode lamp generates narrow emission lines of the element which is being measured. This lines should be of sufficient spectral purity to test spectral resolution of our spectroscopic instrument.

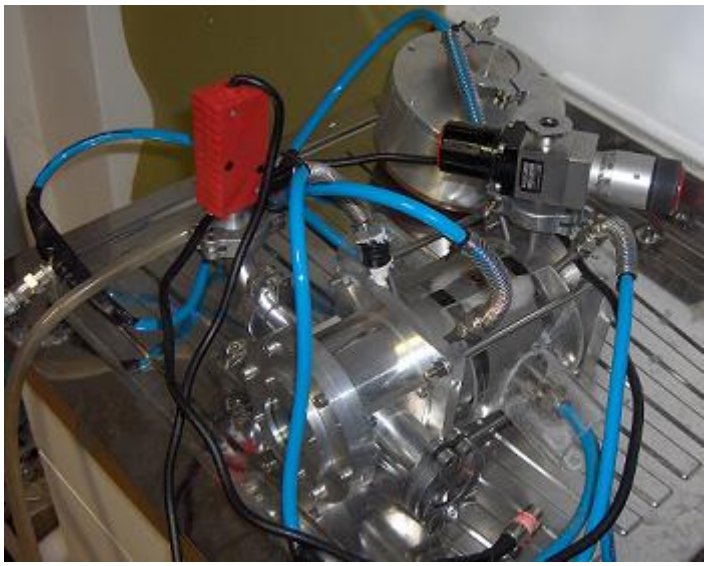

Figure 3.8: Hollow cathode lamp.

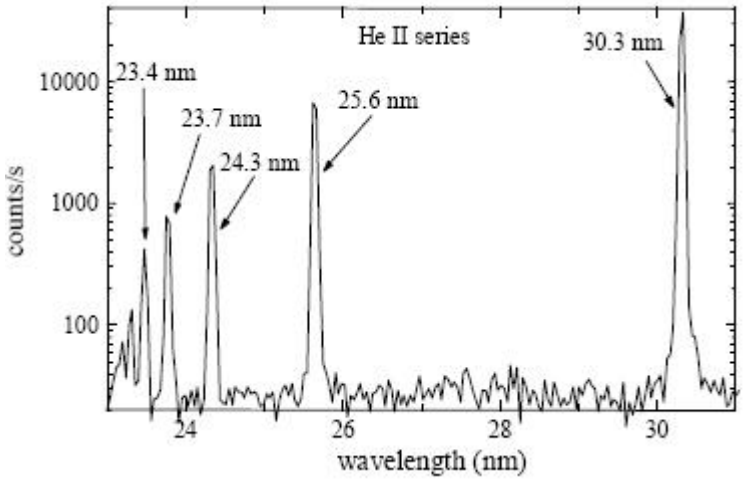

Figure 3.9: Helium filled lamp's spectrum. The region around 23-30 nm is rappresented.

Chapter 4

Experimental Activity

The aim of the experimetal activity is to acquire specifics spectra images that could allow us to conclude that the imaging properties of the instrument are in agreement with simulations. In particular, the activity has been developed in three parts:

- Spectral characterization;
- Spatial characterization on-axis;
- Spatial characterization off-axis.

To test spatial imaging properties of the instrument a spatial slit (perpendicular to the spectral slit) is placed ahead the instrument.

The spectra have been acquired with a detector, contained in a fully integrated camera system. It consists in a back illuminated CCD array with a pixel dimension of 20 μm $\times$ 20 μm. Dark current can be reduced in the camera systems through thermoelectric cooling of the CCD arrays. Obviously, to prevent condensation and contamination from occurring, when cooled the camera must to be operated in vacuum. Data are thus transmitted to a pc. WINSPEC dedicated software is used for the acquisition; it displays the real-time spectral data in graphical format, which can be saved as a bitmap image. From the analysis of these spectra and from the comparison to the simulations we have taken informations relatively spectral and spatial resolution performed by the instrument. These simulations have been made with ZEMAX ray-tracer simulator. The use of ray-tracing techniques can provide a general method for evaluating complex systems in full detail like the instrument we have discussed. In Fig. 4.1, the experimental set-up is showed.

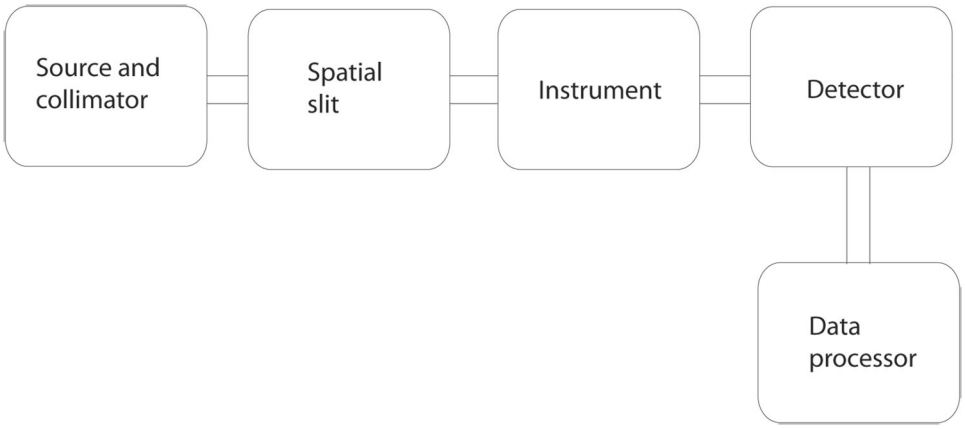

Figure 4.1: Experimental set-up. A spatial slit is placed ahead the instrument to test spatial imaging properties of the instrument. The spectra are acquired with a detector; data are thus transmitted to a pc.

4.1 Spectral characterization

The aim of this part of the experimental activity is to demonstrate that spectral properties of the instrument are in agreement with theoretical simulations. Spectral properties of the instrument depends exclusively on the grating; this has been precedently characterized and tested both in our lab and at the BW3 synchrotron beam-line at DORIS storage ring at DESY campus in Hamburg (Germany). The efficiency curve referred to the first diffractive order (see Appendix A.5.1) is presented in Fig. 4.2 a): the maximum efficiency is 18 %, and is obtained at about 11 nm. In the spectral interval 6,30 nm the efficiency is higher than 5 %. The contribution of the higher orders, compared to the first one, are shown in Fig. 4.2 b). To demonstrate by ourself the good focalization properties of this element, several spectral pictures on axis has been acquired. From this picture we have taken informations relatively the spectral properties performed by the instrument.

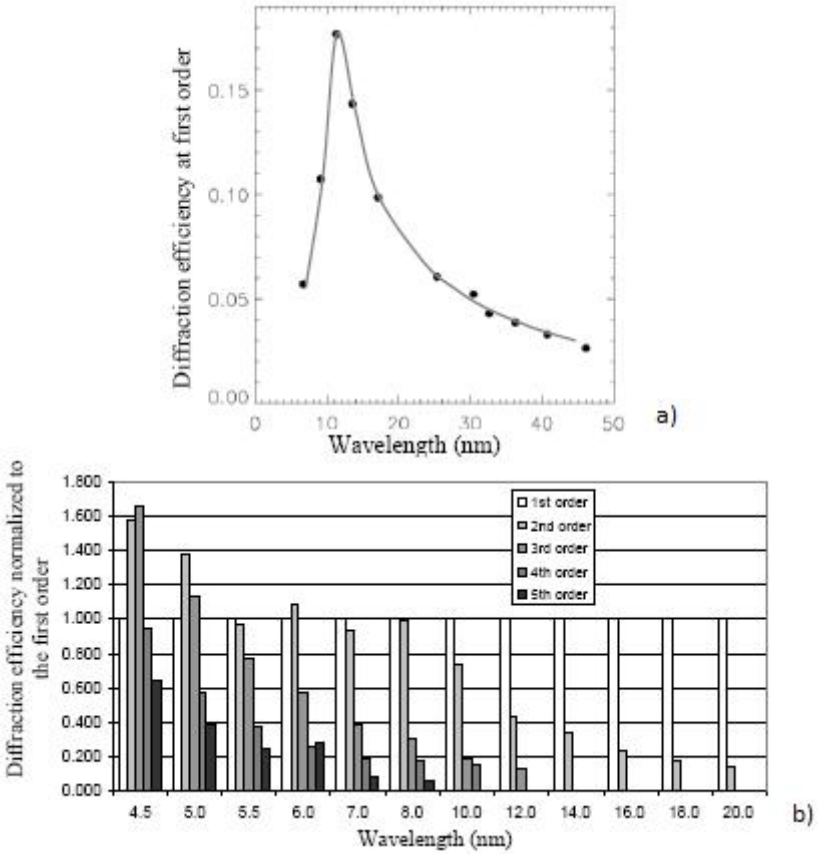

Figure 4.2: a) Grating diffraction efficiency at first order. b) Diffraction efficiency at higher orders compared to the first one.

In Fig. 4.3 and 4.4 are presented two different spectral images acquired on the detector plane at two different apertures of the spectral slit.

Figure 4.3: Helium-filled lamp's spectrum with a spectral slit aperture of 100 μm.

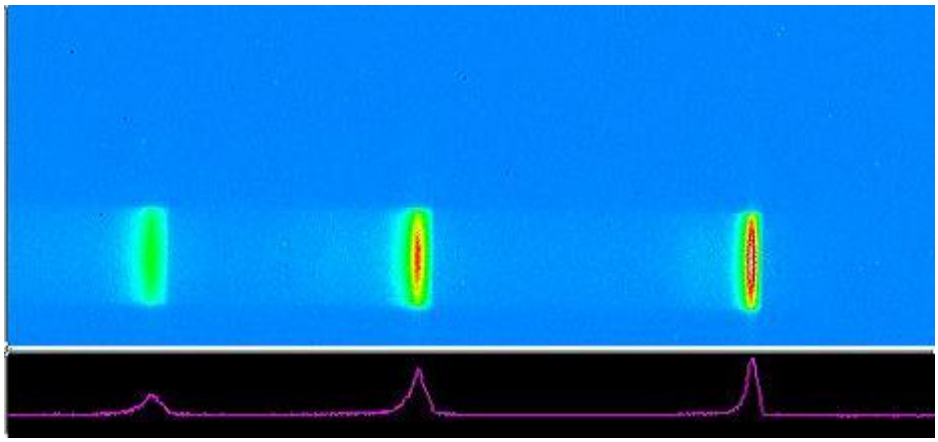

Figure 4.4: Carbon-anode Manson source's spectrum with a spectral slit aperture of 300 μm. The three diffraction orders are visible, the first and most intense is on the right.

The Fig. 4.3 is referred to the first diffractive order of an hollow cathode helium-filled Lamp's spectrum from 30 to 23 nm (starting from left) acquired with an aperture of the spectral slit of 100 μm, while the Fig. 4.4 is referred to the third, second and first diffractive order of a Manson source's spectrum centered at about 6 nm obtained with a carbon anode, aquired with an aperture of the spectral slit of 300 μm. Comparing Fig. 4.3 and Fig. 4.4, the narrower lines of the Helium spectrum respect to the carbon's one are appreciable.

From the observation of these lines we have verified the spectral resolution performed by the instrument comparing the spectral FWHM (see Appendix A.6) of the acquired spectrum with the theoretical FWHM at the same spectral slit's aperture. Theorical simulations performed with ZEMAX ray-tracing software with an aperture of 100 μm gives a value of 3 pixel FWHM, which is in accord with what has been measured. This is enough to allow us to conclude that spectral properties of the instrument are in agreement with simulations.

Particulary interesting is the observation of the spectrum acquired with a Manson source with a silicon anode from 12.5 nm to 16 nm. The spectrum is presented in Fig. 4.5; The image of the spectrum results compatible with what is reported in literature [6].

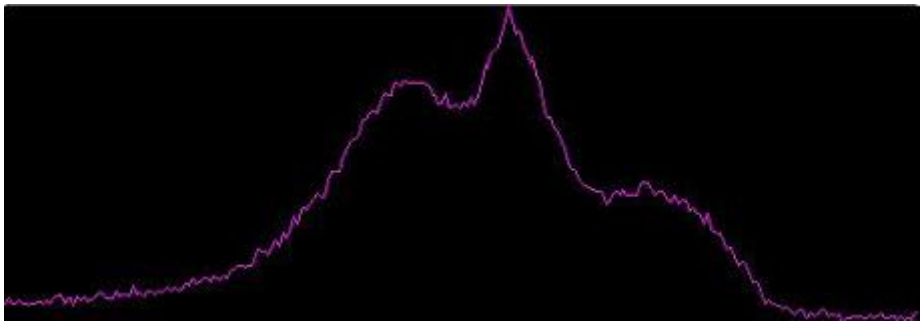

Figure 4.5: Silicon-anode Manson source's spectrum with a spatial slit aperture of 100 μm and a spectral slit aperture of 300 μm.

It is interesting to note that spectral properties of the instrument are not influenced by spatial imaging properties, infact, for a given aperture of the spectral slit the variation of the aperture of the spatial slit, do not alterate the spectral width of the image. To demonstrate it, different images of a Carbon-anode Manson source's spectrum acquired at different aperture of the spatial slit for a given aperture of the spectral slit on the detector plane are presented in Fig. 4.6, 4.7, 4.8. For each image, spectral FWHM of the first order is maintained at a value of 16 pixels. This confirm the spatial-spectral uncouplement properties of the instrument.

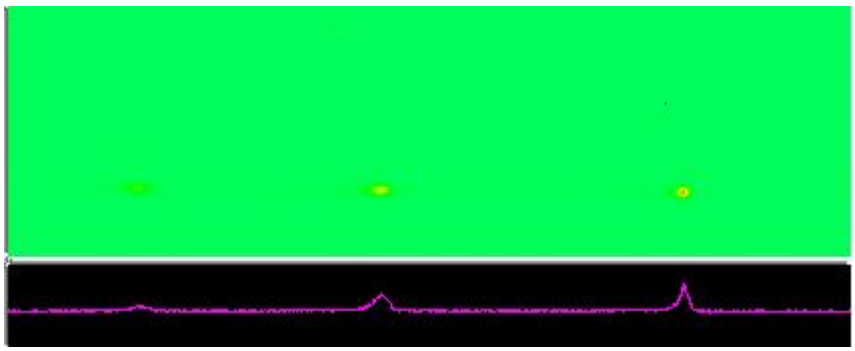

Figure 4.6: Carbon-anode Manson source's spectrum with a spatial slit aperture of 100 μm and a spectral slit aperture of 300 μm.

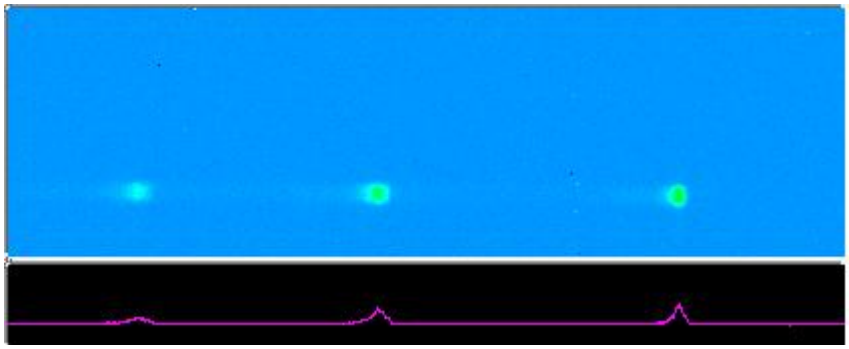

Figure 4.7: Carbon-anode Manson source's spectrum with a spatial slit aperture of 200 μm and a spectral slit aperture of 300 μm.

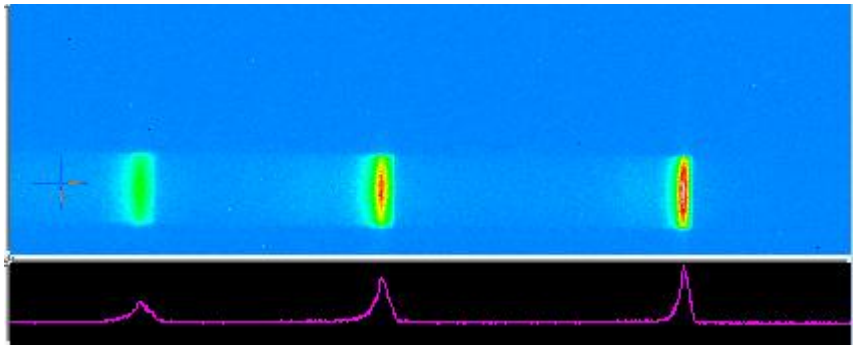

Figure 4.8: Carbon-anode Manson source's spectrum with a spatial slit aperture of 400 μm and a spectral slit aperture of 300 μm.

4.2 Spatial characterization on-axis

The aim of this part of the experimental activity is to demonstrate that the on-axis imaging properties of the instrument are in agreement with simulations. To reach this goal, on-axis pictures at differents apertures of the spatial slit on the detector plane have been acquired. From these pictures we have taken information about the on-axis spatial imaging performed by the instrument.

In Fig. 4.9, 4.10, 4.11 are presented some spectral images acquired at different aperture of the spatial slit on the detector plane, useful for some preliminary considerations. The acquired images are deliberately oversaturated with an apposite choice of the acquisition dinamic. This makes easiest a first approssimative observation of the variation of the spatial width of the acquired spectrum. In this part of the experimental activity, to control the amount of light entering the system, a 4 mm diameter iris is placed in front of the spatial slit. This solution limits the entity of the aberrations because the illuminated area of the optical components is decreased.

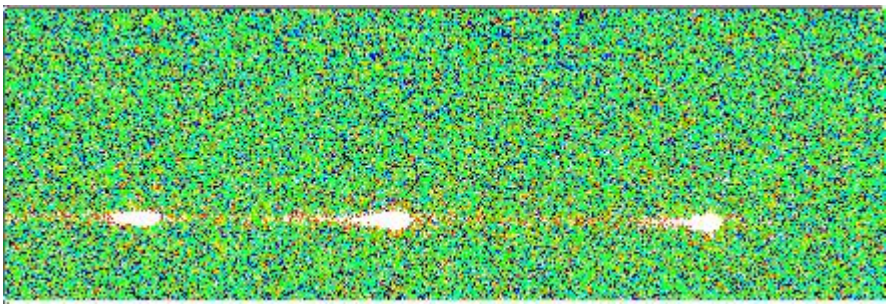

Figure 4.9: Carbon-anode Manson source's spectrum with a spatial slit aperture of 50 μm.

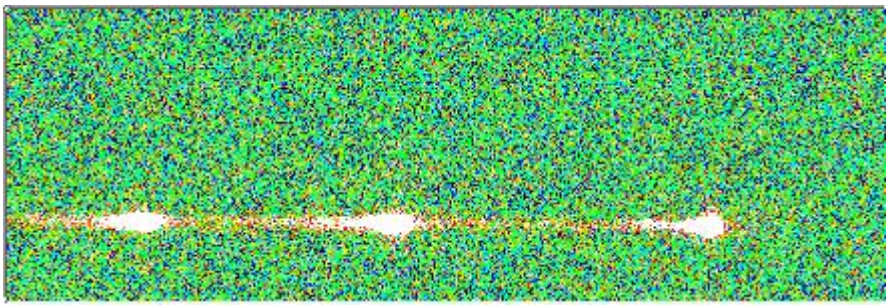

Figure 4.10: Carbon-anode Manson source's spectrum with a spatial slit aperture of 100 μm.

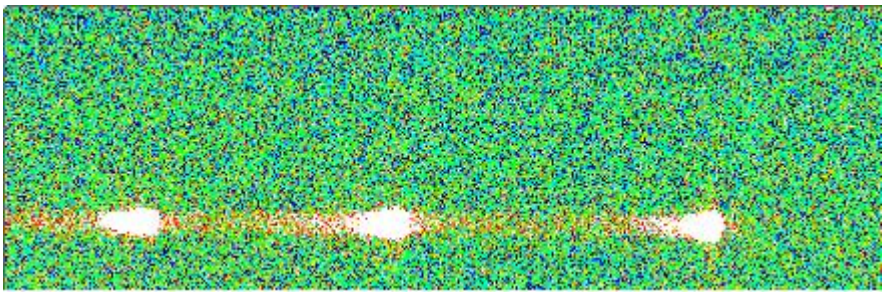

Figure 4.11: Carbon-anode Manson source's spectrum with a spatial slit aperture of 200 μm.

The images reported in Fig. 4.9, 4.10, 4.11 are referred to the third, second and first diffractive order (starting from left) of a Manson source's spectrum centered at 6 nm obtained with a Carbon anode, aquired with three different apertures of the spatial slit on the detector plane: 50 μm-100 μm-300 μm.

We've already concluded that spatial imaging properties are not influenced by spectral properties; the knowing of the spectral slit aperture is so not important for this purpose (only for title of information the spectral slit apertures in Fig. 4.9, 4.10, 4.11 are all of 200 μm); First of all, we can note that the spatial width defined at FWHM (see Appendix A.6) of the images increases for higher values of the aperture of the spatiall slit: this is, for a first observation, in agreement with what the instrument should perform.

Different sources have been employed to analyze with accuracy the on-axis imaging properties of the instrument. In the Table 4.1 we present a comparison between the FWHM of the theoretically simulated spatial width using ZEMAX ray-tracing software and the measured spatial width of the spectra acquired at different aperture of the spatial slit with three different sources: carbon-anode Manson source (which spectrum's image are presented in Fig. 4.9, 4.10, 4.11), silicon-anode Manson source and hollow cathode helium-filled lamp.

Table 4.1: A comparison between the FWHM of the theoretically simulated spatial width using ZEMAX ray-tracing software and the measured spatial width of the spectra acquired on-axis at different aperture of the spatial slit with three different sources.

MANSON SOURCE CARBON ANODE

Aperture [μm]	**The. FWHM [pixel]**	**Mea. FWHM [pixel]**
50	8	11
100	14	14
200	27	27

MANSON SOURCE SILICON ANODE

Aperture [μm]	**The. FWHM [pixel]**	**Mea. FWHM [pixel]**
50	8	7
100	14	12
200	27	30

HOLLOW CATHODE HELIUM FILLED LAMP

Aperture [μm]	**The. FWHM [pixel]**	**Mea. FWHM [pixel]**
50	8	6
100	14	12
200	27	31

We have presented only aperture values from 50 to 400 μm because for lower values e have not sufficient photon flux to deduct accurate information and for higher values optical aberrations are too much important to discriminate authentic data from misinformation.

From the analysis of these data, we can conclude that theoretical simulation of spatial width (defined as FWHM) are in agreement with the measured values of spatial width.

4.3 Spatial characterization off-axis

The aim of this part of the experimental activity is to demonstrate that the spatial imaging properties off-axis of the instrument (for angles from $-0,25°$ to $+0,25°$) are in agreement with simulations. To reach this target, pictures off-axis at differents apertures of the spatial slit on the detector plane has been acquired. From this picture we have taken informations relatively the spatial imaging off axis performed by the instrument.

In Fig. 4.12, 4.13, 4.14 are presented some spectral images acquired at a given aperture of the spatial slit at off-axis angles of $0°, \pm 0.25°$ on the detector plane, useful for some preliminary considerations. Like the previous part of the experimental activity, the acquired images are deliberately oversaturated and a 4 mm diameter iris is placed in front of the system. It is possible to note that images are rotated of 90 degrees respect the previous acquisitions; This is because the dector has been rotated to obtain a greater range of sight.

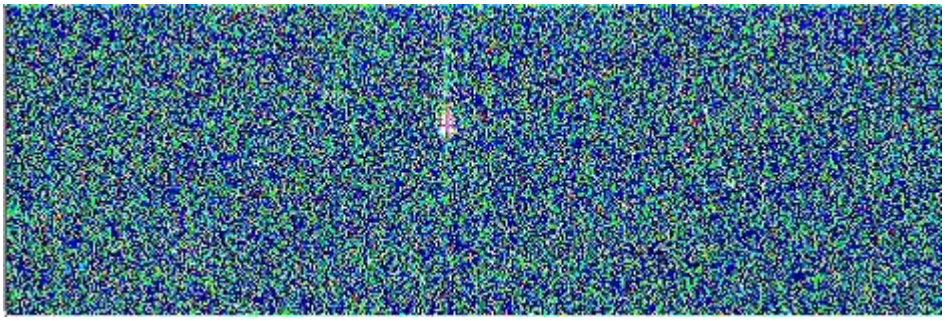

Figure 4.12: Carbon-anode Manson source's spectrum with a spatial slit aperture of 100 μm and a $0°$ tilt.

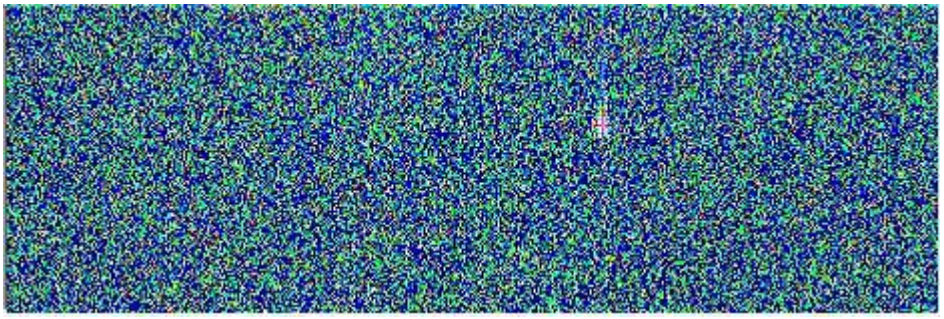

Figure 4.13: Carbon-anode Manson source's spectrum with a spatial slit aperture of 100 μm and a $-0.25°$ tilt.

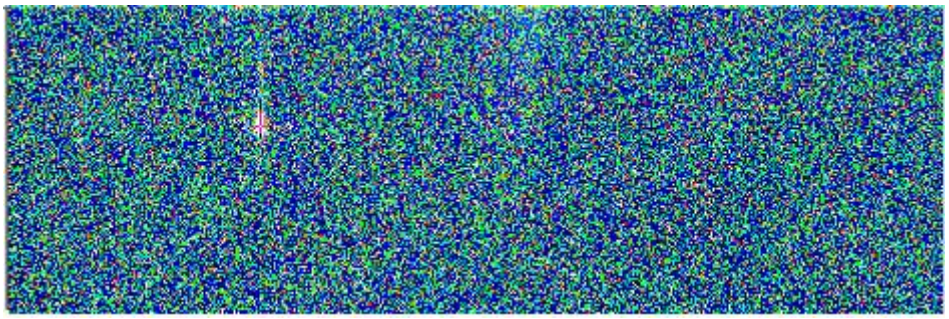

Figure 4.14: Carbon-anode Manson source's spectrum with a spatial slit aperture of 200 μm and a $+0.25°$ tilt.

First of all, we can note that for off-axis angles takes place a displacement of the acquired spectrum in the spatial direction (upwards for negative tilts, downward for positive tilts). It is important to note that the displacement is larger for positive tilts, due to the not symmetrical telescope arrangement respect to the on axis propagating beam. Infact, the theorical value of the $-0,25°$ displacement respect to the axis is 5.286 mm, while the theorical value of the $+0,25°$ displacement respect to the axis is 5.563 mm.

Then, it is evident that the spatial width defined as FWHM of the images do not present increasement for off-axis angles and that the imaging properties of the instrument remains inalterated; this is, for a first observation, in agreement with what the instrument should perform.

Different spectra at different off-axis angles have been acquired to analyze with accuracy imaging properties off-axis of the instrument. In the Table 4.2 we present a comparison beetwen the FWHM theoretically simulated spatial width using ZEMAX ray-tracing software and the measured spatial width of the image at different aperture of the spatial slit for different off-axis angles: $0°, \pm 0.125° \pm 0.25°$. All spectra presented have been originated from a Carbon-anode Manson source.

Table 4.2: A comparison between the FWHM of the theoretically simulated spatial width using ZEMAX ray-tracing software and the measured spatial width of the spectra acquired at different aperture of the spatial slit for different off-axis angles.

SPATIAL SLIT APERTURE 50 μm

Tilt [°]	**The. FWHM [pixel]**	**Mea. FWHM [pixel]**
+0.125	8	12*
+0.25	8	8
0	8	11
-0.125	8	16*
-0.25	8	9

SPATIAL SLIT APERTURE 100 μm

Tilt [°]	**The. FWHM [pixel]**	**Mea. FWHM [pixel]**
+0.125	14	12
+0.25	14	11
0	14	14
-0.125	14	14
-0.25	14	19

SPATIAL SLIT APERTURE 200 μm

Tilt [°]	**The. FWHM [pixel]**	**Mea. FWHM [pixel]**
+0.125	27	34*
+0.25	28	28
0	27	27
-0.125	27	42*
-0.25	28	34

SPATIAL SLIT APERTURE 400 μm

Tilt [°]	**The. FWHM [pixel]**	**Mea. FWHM [pixel]**
+0.125	54	59
+0.25	55	58
0	53	70*
-0.125	54	64
-0.25	55	70*

The use of the 4 mm diameter iris take us to conclude with sureness that our spots are not dominated by aberrations but, unfortunately, there are some values that are not in agreement with simulations. This behaviour is probably determinated by the difficult of an appropriate tilt of the instrument, due to our limited resources; It is possible that some optical component of the instrument suffered a disalignment, originating an improper appreciation of the spatial FWHM performed by the instrument. We've denoted with asterisks the values of FWHM for which this phenomenon is more evident. Unfortunely, it results impossible to conclude if simulations of spatial width defined at FWHM are in agreement with these measured values of spatial width defined at FWHM. In near future, it would be very gratifying to try the acting of an appropriate tilt in a dedicated facility.

Chapter 5

Conclusions and future trends

Spectral properties of the instrument have been measured and compared with theoretical spectral properties. From the analysis of the measured values it is possible to conclude that spectral properties of the instrument are in agreement with theoretical simulations.

Spatial imaging properties on-axis of the instrument have been measured and compared with theoretical spatial imaging properties on-axis. From the analysis of the measured values it is possible to conclude that spatial imaging properties on-axis of the instrument are in agreement with theoretical simulations.

Spatial imaging properties off-axis of the instrument have been measured and compared with theoretical spatial imaging properties off-axis. Unfortunely, it is impossible to conclude that spatial imaging properties off-axis of the instrument are in agreement with theoretical simulations. In near future, it would be very gratifying to try the acting of an appropriate tilt in a dedicated facility.

Appendix

Appendix A

A.1 XUV and Soft X-Ray regions

UV spectrum is the region of the electromagnetic spectrum which extends from about 400 nm to about 10 nm. More specifically: Near UltraViolet (NUV) comprises wavelength from 400 nm to 300 nm, Middle UltraViolet (MUV) from 300 to 200 nm, Far UltraViolet (FUV) from 200 nm to 120 nm and eXtreme UltraViolet (XUV) comprises wavelength from 120 nm to 10 nm. Due to high absorption of air below to 200 nm the region from 200 nm to 10 nm is also called Vacuum UltraViolet because radiation can propagate only in vacuum.

X-ray region is the region of the electromagnetic spectrum which extends from about 10 nm to 0.01 nm. X-rays from about 10 nm to 0.1 nm are classified as soft X-rays, and from about 0.1 nm to 0.01 nm as hard X-rays, due to their penetrating abilities (See Fig. A.1).

XUV and soft X-ray are particular regions of the spectrum because no refractive materials transmit radiation of this wavelengths and it results also necessary working at grazing incidence because the reflectivity at these wavelengths is very small at normal incidence. In Fig. A.2 are reported typical values of reflectivity for Carbon and Silicon as the wavelength changes, for different angles beetwen 20 ° to 0.5 °. It is evident that for higher values of the photon's energy (and thus for smaller values of the wavelength) the reflectivity is greater for small angles.

Spectroscopy in any spectral region requires the use of optical components that disperse the radiation into a spectrum and deflect and focus light to form images. In visible an IR spectroscopy both prisms an gratings can be used for this purpose but at wavelengths ranging from XUV to X-ray only reflective gratings are available because it is impossible to work in transmition. For the same reason, it is not possible to use lenses in this spectral domain.

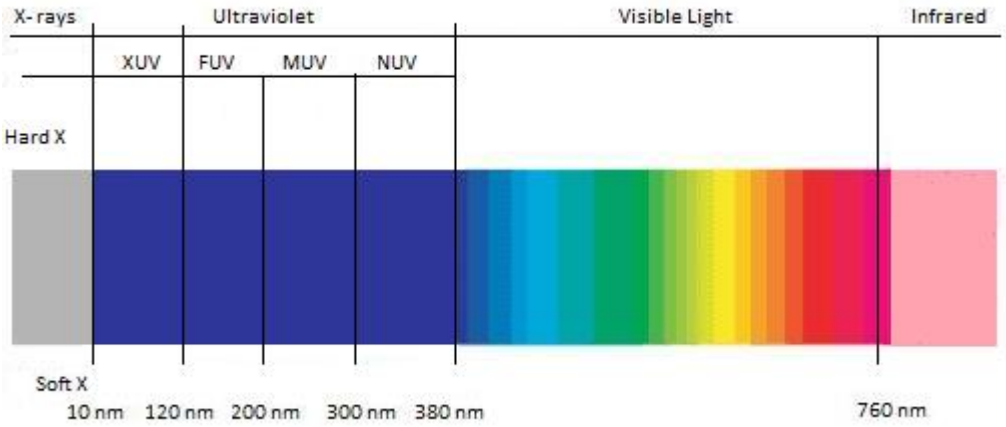

Figure A.1: UV and X-ray electromagnetic spectrum. XUV and Soft X-ray region are observable.

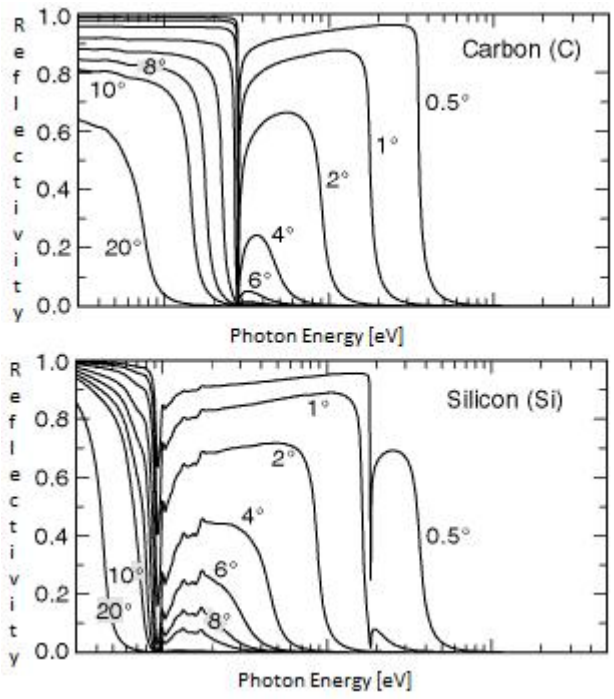

Figure A.2: Reflectivity for Carbon and Silicon as the wavelength changes, for different angles beetwen 20 ° to 0.5 °.

A.2 Aberrations

Paraxial approximation is based on the assumption that rays propagate very close to the optical axis; thus the system is restricted to work in a narrow region around the optical axis. When we consider also rays from the periphery of the optical element, the approximation $sin\alpha \simeq \alpha$ falls down. It results necessary taking other terms of the expansion series of the sin function:

$$sin\alpha = \alpha - \frac{\alpha^3}{3!} + \frac{\alpha^5}{5!} - \frac{\alpha^7}{7!} + ... \tag{A.1}$$

If the first two terms are retained we have the so called third order theory. Departures from first order theory that results are embodied in five primary aberrations: spherical aberration, coma, astigmatism, field curvature and distorsion.

In this section we are going to explain the meaning of these five aberrations.

- **Spherical aberration:** it corresponds to a dependence of focal length on aperture for non paraxial rays. Rays striking the surface at greater distance from the axis are focused nearer the vertex. Spherical aberration pertains only to object points that are on the optical axis. The distance between the axial intersection of a ray and the paraxial focus is known as Longitudinal Spherical Aberration (LSA). If a screen is placed at the paraxial focus, the image of a point source will appear as a bright central spot on the axis surrounded by a halo (see Fig. A.3). The height above the axis where a given ray strikes this screen is called the Transverse Spherical Aberration (TSA). There is a point on the axis in which the image blur has its smallest diameter; this is known as the circle of least confusion and the corresponding position is generally the best place to observe the image. For an extended image, spherical aberration would reduce the contrast and degrade the details. It can be reduced by stopping down the aperture, but that reduces the amount of light entering the system as well.

- **Astigmatism:** when an object point lies on an appreciable distance from the optical axis, the incidence rays will strike the optic asymmetrically, giving rise to astigmatism. This aberration becomes important when inclination of the bundle of rays predominates over its aperture. Astigmatism is better understandable if we introduce the concept of tangential and sagittal planes. The tangential plane is the plane containing both the chief ray and the optical axis; the sagittal plane is the plan that contains the chief ray and that is perpendicular to the tangential plane. In the case of an axial object point, the cone of rays is symmetrical with respect to the spherical surface. The ray

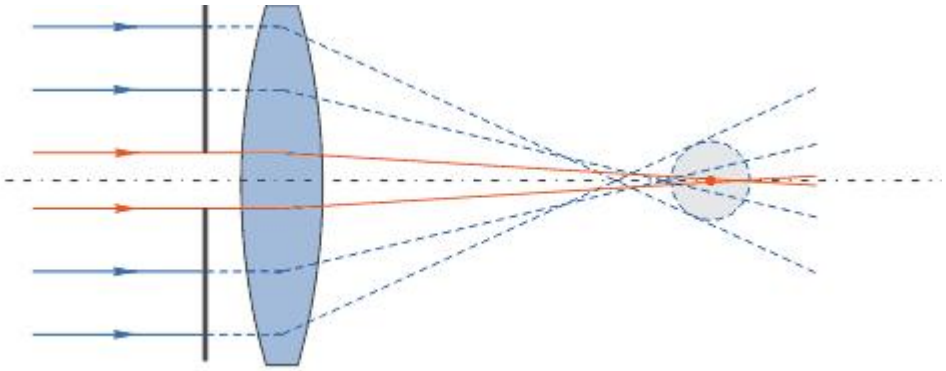

Figure A.3: Spherical aberration. It is observable the dependence of the focal length on aperture for non paraxial rays. Rays striking the surface at greater distance from the axis are focused nearer the vertex.

configuration in all planes containing the optical axis are identical. In the absence of spherical aberration, all the focal lengths are the same, and consequently all rays arrives at a single focus. In contrast, the configuration of an oblique, parallel ray bundle will be different in the tangential and sagittal planes. As result, the focal lengths in this planes will be different as well. In effect, the tangential rays are tilted more with respect to the mirror than the sagittal rays, and they have a shorter focal length. This astigmatic difference, increases rapidly as the rays become more oblique, and is zero on axis. We have thus two focal lengths, one for the tangential rays and one for the sagittal rays, in which the cone of rays focuses in two orthogonal segments (see Fig. A.4). Between the tangential and the sagittal focus there is a location in which the beam's cross section is circular, the circle of least confusion. Since this circle increases in diameter as the astigmatic difference increases, the image will be more deteriorated, losing definition around its edges.

- **Coma:** it arises from the fact that the transverse magnification differs for rays striking off-axis regions of the mirrors. The net result is that an off-axis object point is imaged in a geometrical figure which somewhat resembles the shape of a comet, a coma (see Fig.A.5). The figure of aberration is observable if the object is not at infinite, but the aperture of the bundle of rays must prevail over its inclination.

- **Field Curvature:** it refers to the fact that a planar object point is imaged approximately as a plane only in the paraxial region. At finite apertures the imaging process results in a curved stigmatic image surface.

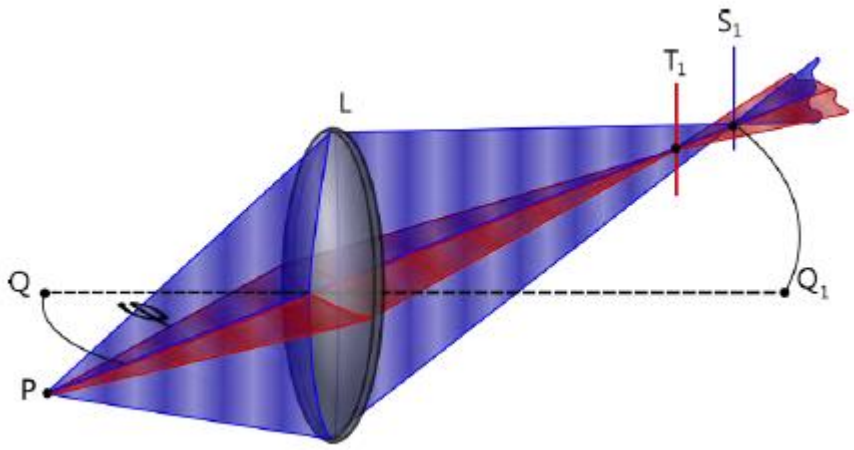

Figure A.4: Astigmatism. Two focal lengths are observable, one for the tangential rays (T) and one for the sagittal rays (S), in which the cone of rays focuses in two orthogonal segments.

- **Distorsion:** it is originated from the fact that the transverse magnification may be a function of the off-axis image distance. Different areas of the mirrors have different focal length and different magnifications. Distorsion manifests itself as a whole misshaping of the image, altought each point is well focused.

  Obviously, it is important to adopt optical systems that reduces this kind of optical defects, because they degrades the quality of the image and thus the instrument's performance [7].

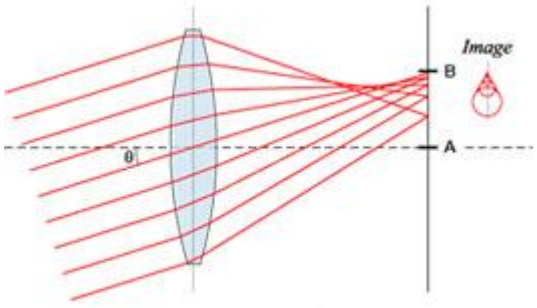

Figure A.5: Coma aberration. An off-axis object point is imaged in a geometrical figure which somewhat resembles the shape of a coma.

A.3 Mirrors in XUV and X-ray domains

Mirrors are portion of reflecting surfaces which, by means of reflecting rays of light, either revert optical bundles or focus them to form images. We assume that basic concepts of geometrical optics, such as conjugate points, focal distances, principal planes and so on, are well known. It is important to remember that XUV and soft X-ray are particular regions of the spectrum because we cannot work at normal incidence due to low reflectivity at this wavelength; so it is necessary to work at grazing incidence. The interaction of UV and soft X-rays with matter can infact be described by the complex index of refraction of the reflector:

$$n = 1 - \delta - i\beta = \sqrt{\epsilon}, \tag{A.2}$$

where δ describes the phase change and β accounts for the absorption. Instead of the index of refraction the complex dielectric constant ϵ may be used. The reflection coefficients for p and s polarisation are given by the Fresnel equations:

$$r_p = \frac{E_R}{E_{I\ p}} = \frac{n^2 sin\alpha - \sqrt{(n^2 - cos^2\alpha)}}{n^2 sin\alpha + \sqrt{(n^2 - cos^2\alpha)}}, \tag{A.3}$$

$$r_s = \frac{E_R}{E_{I\ s}} = \frac{sin\alpha - \sqrt{(n^2 - cos^2\alpha)}}{sin\alpha + \sqrt{(n^2 - cos^2\alpha)}}. \tag{A.4}$$

E_R/E_I denotes the ratio of the amplitudes of the reflected and incident electric fields and α is the grazing angle of incidence as measured from the interface plane. This approach is, in principle, correct as long as the assumptions inherent in the Fresnel equations are fulfilled: the reflector is assumed to have a perfectly flat surface and its atomic structure scales are small compared to the wavelength used. The reflected intensity or reflectivity is then $R_p = r_p r_p^*$ and $R_s = r_s r_s^*$, where the asterisk denotes the conjugate complex value. In the case of incident unpolarised x-rays the reflectivity is $R = (R_p + R_s)/2$. Since the real part of n is less than unity for matter at these wavelengths, total external reflection occurs at a grazing angle α_t, according to Snell's law:

$$cos\alpha_t = 1 - \delta, \tag{A.5}$$

or for $\delta << 1$:

$$\alpha_t = \sqrt{2}\delta. \tag{A.6}$$

Because of the non-vanishing value of β the reflection is actually not total for $\alpha \leq \alpha_t$, but is less than unity, and x-rays are reflected at incident angles even larger than the critical angle α_t.

The index of refraction or the optical constants can be computed from anomalous dispersion theory. For XUV and soft X-ray wavelengths λ sufficiently apart from absorption edges δ reads as follows:

$$\delta = N_0 \frac{Z r_e}{A 2\pi} \rho \lambda^2, \tag{A.7}$$

where N_0 is Avogadro number, r_e is the classical electron radius, Z and A are the atomic number and weight, respectively, and ρ is the mass density. In the case of heavy elements, for which Z/A is about 0.5, the critical angle for $\delta << 1$ can be estimated:

$$\alpha_t = 5.6\lambda\sqrt{\rho}, \tag{A.8}$$

with α_t, in arcmin, δ in $\dot{A}$ and ρ in g/cm^3. This means that for x-rays with a wavelength of a few amstrongs the critical angle is about one degree. Equation (A.8) also shows the superiority of heavy elements as reflectors in these wavelengths. Therefore, mirrors for this domain must be then made of (or coated with) reflective heavy materials. Metallic coatings are commonly used. Best reflectors are the heaviest metals such as gold and platinum [8].

A.4 Optical configurations for our purpose

A critical problem working in grazing incidence is the presence of optical aberrations. Optical configurations of plane, spherical or toroidal mirrors, cannot provide imaging without aberration. It results fundamental the use of optical configuration based on quite complex optical surfaces that allows a better imaging. These surfaces are conical surfaces with axial symmetry: the ellipse, the parabola and the hyperbole (see Fig. A.6) [9].

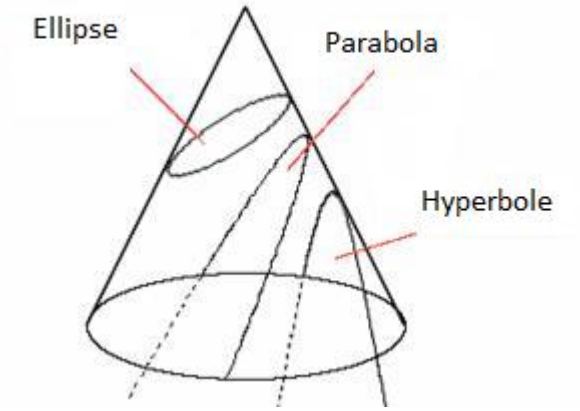

Figure A.6: Ellipse, parabola and hyperbole.

There are many types of optical configuration using these particular surfaces. They can be distinguished by the geometry and arrangement of the mirror substrates used, e.g. Kirkpatrick-Baez configuration and Wolter configuration.

A.4.1 Kirkpatrick-Baez configuration

Kirkpatrick-Baez-optics consist of a set of two orthogonal mirrors, of which incident rays are reflected successively. The surface of the first mirror is aligned perpendicullary to the second mirror's surface. In order to achieve a common focal point, both mirrors have to be curved elliptically in a way, that leads go the horizontal focus line of the first mirror and the vertical focus line of the second mirror coinciding in the same plane (see Fig. A.7). In practical designs, the surface area is increased by using many approximately parallel mirrors (i.e., nesting) in each reflecting stage. The Kirkpatrick-Baez system offers inexpensive construction since the reflecting surfaces can be optically flat glass plates, bent to the proper curvature by mechanical stressing.

On the other hand, the coalignment of many reflecting surfaces to form an optimum image is a difficult process [9].

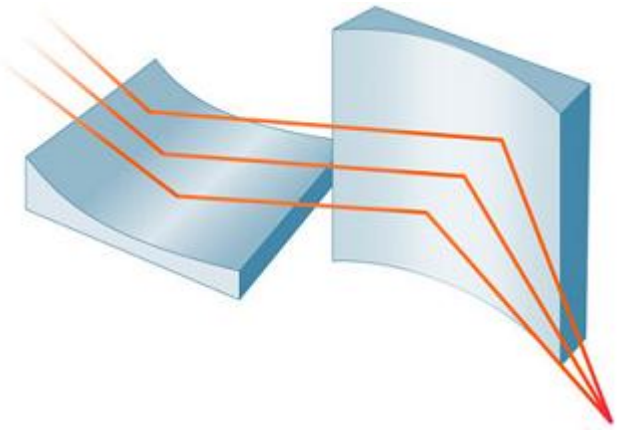

Figure A.7: Kirkpatrick-Baez configuration.

A.4.2 Wolter configurations

Wolter configurations are designed only for grazing incidence optics, and they are usually employed for the realization of telescopes. Wolter described three different imaging configurations, the Types I, II, and III (see Fig.A.8). The design most commonly used for XUV and soft X-ray application is the Type I since it has the simplest mechanical configuration. In addition, the Type I design offers the possibility of nesting several telescopes inside one another, thereby increasing the useful reflecting area. This is an extremely important attribute, as virtually all X-ray sources are weak, and maximizing the light gathering power of a mirror system is critical. For comparable apertures and grazing angles, the primary advantage of Type II over Type I is that higher focal plane magnifications are attainable. This is so because the second reflection is off the outside of a surface, thus allowing longer focal lengths. However, since off-axis images suffer much more severely from blurring in Type II configurations, the Wolter Type II is useful only as a narrow-field imager or as the optic for a dispersive spectrometer. The Wolter type III is not commonly used for XUV and soft X-ray application and has never been used for X-ray astronomy [9].

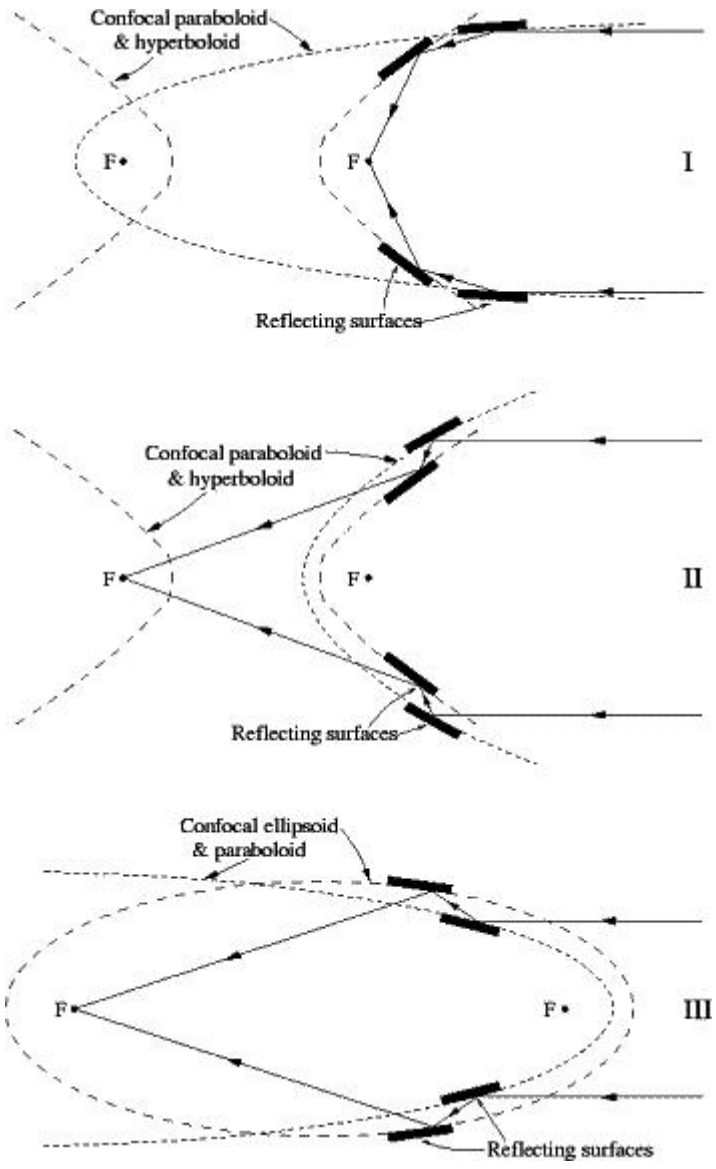

Figure A.8: Wolter I,II,III Telescopes.

A.5 Grazing incidence grating

As also explained, the greatest issue in XUV spectroscopy is the impossibility to use transmission optics. As a consequence, in the design of a spectrograph or monochromator, one cannot make use of lenses in order to focus the spectrum into the exit slit. The solution is given by using a concave reflecting grating, obviously at grazing incidence. A concave diffraction grating is an optical component with a concave structure (usually spherical or toroidal), which splits and diffracts light into several beams travelling in different directions depending on the wavelengths of the light, regardless of its groove pattern, profile, or the mount in which it is used. Examples are spherical substrates (whose surfaces are portions of a sphere, which are definable with one radius) and toroidal substrates (definable by two radii). Spherical substrates are by far the most common type of concave substrates, since they are easily manufactured and toleranced, and can be replicated in a straightforward manner. Toroidal substrates are much more difficult to align, tolerance and replicate, but astigmatism can generally be corrected better than by using a spherical substrate. More general substrate shapes are also possible, such as ellipsoidal or paraboloidal substrates, but tolerancing and replication complications relegate these grating surfaces out of the mainstream. Moreover, the use of aspheric substrates whose surfaces are more general than those of the toroid do not provide any additional design freedom for the two lowest-order aberrations (defocus and astigmatism). The shape of a concave grating (considering only spheres and toriods) can be characterized either by its radii or its curvatures. The radii of the slice of the substrate in the principal (dispersion) plane is called the tangential radius R, while that in the plane parallel to the grooves at the grating center is called the sagittal radius. A plane grating is one whose surface is planar. Plane gratings can be thought of as a special case of concave gratings (for which the radii of curvature of the substrate become infinite).

A classical grating is one whose grooves, when projected onto the tangent plane, form a set of straight equally-spaced lines. Until the last few decades, the vast majority of gratings were classical, in that any departure from uniform spacing, groove parallelism or groove straightness was considered a flaw.

A varied line-space (VLS) grating is one whose grooves, when projected onto the tangent plane, form a set of straight parallel lines whose spacing varies from groove to groove. Varying the groove spacing across the surface of the grating moves the tangential focal curve, while keeping the groove straight and parallel keeps the sagittal focal curve fixed [9].

A.5.1 Physics of a generic diffraction grating

When monochromatic light is incident on a grating surface, it is diffracted into discrete directions. We can picture each grating groove as being a very small, slit-shaped source of diffracted light. The light diffracted by each groove combines to form set of diffracted wavefronts. The usefulness of a grating depends on the fact that there exists a unique set of discrete angles along which, for a given spacing d between grooves, the diffracted light from each facet is in phase with the light diffracted from any other facet, leading to constructive interference.

Diffraction by a grating can be visualized from the geometry in Fig. A.9, which shows a light ray of wavelength λ incident at an angle α and diffracted by a grating (of groove spacing d) along at set of angles β_m. These angles are measured from the grating normal, which is shown as the dashed line perpendicular to the grating surface at its center. The sign convention for these angles depends on whether the light is diffracted on the same side or the opposite side of the grating as the incident light. In Fig. A.6, which shows a reflection grating, the angles $\alpha > 0$ and $\beta_1 > 0$ (since they are measured counter-clockwise from the grating normal) while the angles $\beta_0 < 0$ and $\beta_{-1} < 0$ (since they are measured clockwise from the grating normal).

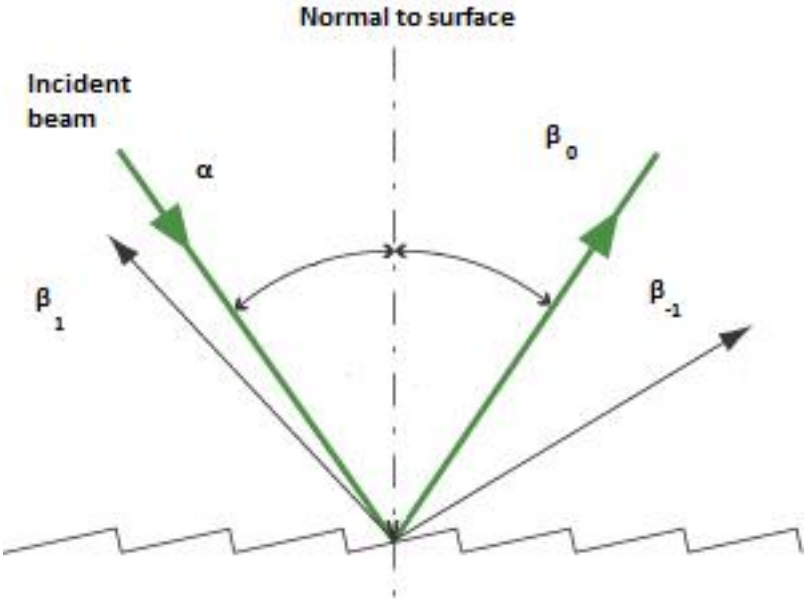

Figure A.9: Grating structure.

The geometrical path difference between light from adjacent grooves is seen to be $dsin\alpha + dsin\beta$. The principle of constructive interference dictates that only when this difference equals the wavelength λ of the light, or some integral multiple thereof, will the light from adjacent grooves be in phase (leading to constructive interference). At all other angles the wavelets originating from the groove facets will interfere destructively.

These relationships are expressed by the **grating equation**:

$$m\lambda = dsin\alpha + dsin\beta, \tag{A.9}$$

where d is the groove spacing, m is the diffraction order, which is an integer. For a particular wavelength λ, all values of m for which $|m\lambda/d| < 2$ correspond to propagating (rather than evanescent) diffraction orders. The case $m = 0$ leads to the law of reflection $\beta = -\alpha$.

The angular spread $\Delta\beta$ of a spectrum of order m between the wavelength λ and $+\Delta\lambda$ can be obtained by differentiating the grating equation, assuming the incidence angle a to be constant. The change Δ in diffraction angle per unit wavelength is called **angular dispersion** and is, therefore:

$$\Delta = d\beta/d\lambda = \frac{m}{dcos\beta}. \tag{A.10}$$

The **resolving power** R of a grating is a measure of its ability to separate adjacent spectral lines of average wavelength λ. It is usually expressed as the dimensionless quantity:

$$R = \frac{\lambda}{\Delta\lambda}, \tag{A.11}$$

where $\Delta\lambda$ is the limit of resolution, the difference in wavelength between two lines of equal intensity that can be distinguished. The theoretical resolving power of a planar diffraction grating is given by the equation:

$$R = mN, \tag{A.12}$$

where N is the total number of grooves illuminated on the surface of the grating.

While resolving power can be considered a characteristic of the grating and the angles at which it is used, the ability to resolve two wavelengths λ_1 and $\lambda_2 = \lambda_1 + \Delta\lambda$, generally depends not only on the grating but on the dimensions and locations of the entrance and exit

slits (or detector elements), the aberrations in the images, and the magnification of the images. The minimum wavelength difference $\Delta\lambda$ between two wavelengths that can be resolved unambiguously, a quantity called **resolution**, can be determined by convoluting the image of the entrance aperture (at the image plane) with the exit aperture (or detector element). This measure of the ability of a grating system to resolve nearby wavelengths is arguably more relevant than is resolving power, since it takes into account the image effects of the system. While resolving power is a dimensionless quantity, resolution has spectral units (usually nanometers).

The distribution of power of a given wavelength diffracted by a grating into the various spectral order depends on many parameters, including the power and polarization of the incident light, the angles of incidence and diffraction, the (complex) index of refraction of the materials at the surface of the grating, and the groove spacing. A complete treatment of **grating efficiency** requires the vector formulation of electromagnetic theory (i.e., Maxwell's equations) applied to corrugated surfaces, which has been studied in detail over the past few decades. While the theory does not yield conclusions easily, certain rules of thumb can be useful in making approximate predictions.

The simplest and most widely used rule of thumb regarding grating efficiency (for reflection gratings) is the blaze condition:

$$m\lambda = 2dsin\theta_B, \tag{A.13}$$

where θ_B (called the blaze angle of the grating) is the angle between the face of the groove and the plane of the grating (see Fig. A.10). When the blaze condition is satisfied, efficiency is enhanced [10].

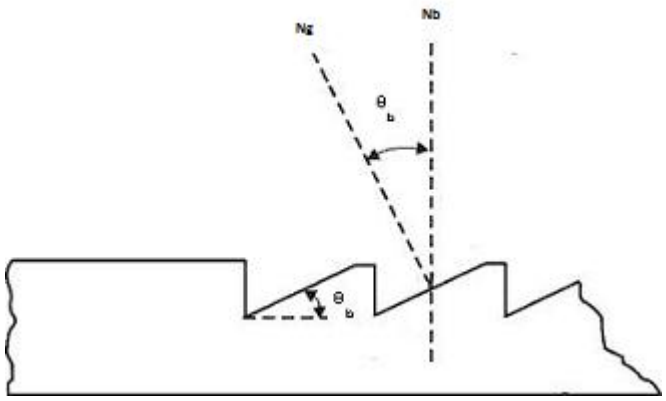

Figure A.10: Blaze angle.

A.5.2 VLS concave grating imaging

The optical layout of a SVLS grating is shown in Fig. A.11: the origin O of the rectangular coordinate system is on the grating vertex, the x axis is normal to the surface at the origin point, and the y and the z axes are perpendicular and parallel, respectively, to the grooves. The source is placed at point $A(x_A, y_A, 0)$ in the x,y plane, and point $B(x_B, y_B, 0)$ is the nominal focal point of wavelength λ diffracted in the m_{th} order by the grating. The generic point $P(x, y, z)$ spans the grating surface.

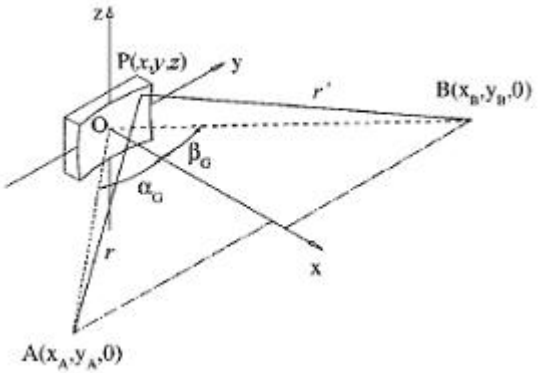

Figure A.11: SVLS optical layout.

The groove density along the grating is expressed as:

$$\sigma(y) = \sigma_0(1 + 2\frac{b_2}{R}y + 3\frac{b_3}{R^2}y^2 + 4\frac{b_4}{R^3}y^3), \tag{A.14}$$

where σ_0 is the central groove density; R is the radius of the grating; and b_2, b_3, b_4 are the ruling parameters for space variation.

We find the relation between the geometrical parameters, which are entrance arm r, exit arm r ', incidence angle α_g , and diffraction angle β_g, and the grating parameters by expressing the light-path function F as a power series of y and z:

$$F = r+r'+yF_{10}+y^2F_{20}+y^3F_{30}+yz^2F_{12}+y^4F_{40}+y^2z^2F_{22}+z^4F_{04}+O(y^6). \tag{A.15}$$

According to Fermat's principle of least time, the image point B is located such that the light-path function will be an extreme for any point P spanning over the grating surface. We then obtain the stigmatic spectral image focusing by setting the derivative with respect

to the variables y and z equal to zero, i.e., $\partial F_y/y = \partial F_z/z = 0$. The latter condition must be satisfied simultaneously by any pair of y and z on the surface of the grating for the fixed point B. This is realized when all coefficients of the power series in the equation are set equal to zero. However, at grazing incidence it is impossible to simultaneously satisfy both the conditions $\partial F_y/y = 0$ and $\partial F_z/z = 0$ with a spherical surface, because the radius adopted to ensure that the tangential focusing properties (i.e., on the plane of the spectral dispersion) provide almost no sagittal focusing capability (i.e., on a plane perpendicular to the plane of the dispersion). To obtain highly spectral resolved images, at best only the tangential aberrations can be minimized following the condition $\partial F_y/y = 0$. The latter is satisfied when all terms F_{n0} of the power series with n 1 are set to 0.

The condition $F_{10} = 0$ gives the grating equation:

$$sin\alpha_g + sin\beta_g = m\lambda\sigma_0. \tag{A.16}$$

Here the signs of α_g andβ_g are opposite if A and B lie on different sides of the x,z plane.

The term F_{20} controls the defocusing along the direction of spectral dispersion; this is the main tangential aberration, which increases linearly with the width of the illuminated area on the grating; we obtain the spectral focal curve, which is the curve where the spectral defocusing becomes zero, by setting F_{20} equal to zero:

$$\frac{cos^2\alpha_g}{r} + \frac{cos^2\beta_g}{r\,'} - \frac{cos\alpha_g + cos\beta_g}{R} + 2(sin\alpha_g + sin\beta_g)\frac{b_2}{R} = 0. \tag{A.17}$$

To minimize the defocusing on the detection system, it is necessary to make the focal curve given by the equation as close as possible to the detector surface in the spectral range of interest. In the design of a spectrograph, some of the parameters, such as the incidence angle, the central groove density, and the entrance and exit arms, are usually given by scientific requirements on spectral resolution and efficiency; the remaining free parameters R and b_2 used to minimize the deviation between the spectral focal curve given by the equation and the detector plane.

Similarly it can be shown that the used to minimize the deviation between the spectral focal curve given by the last equation and the detector plane. Similarly it can be shown that the F_{30} and F_{40} terms, which depend on the parameters b_3 and b_4, respectively, control coma and spherical aberration. An advantage of using a SVLS grating

is that both functions of dispersion and spectral focusing are combined into a single optical element for high throughput. In addition to this, an almost flat focal surface at near-normal incidence with minimum high-order aberrations is obtained. It is then possible to use both microchannel-plate-based and EUV-enhanced CCD detectors with plane surfaces [4].

A.6 FWHM

The intensity distribution of light incoming on the image plane is Gaussian both in the spectral and in spatial directions. The Gaussian distribution is expressed by:

$$f_g(x) = \frac{1}{\sqrt{2\pi\sigma^2}} e^{-\frac{-(x-a)^2}{2\sigma^2}}. \tag{A.18}$$

where parameter a is the mean or expectation, σ^2 is the variance, the mean of the squared deviation, (a "measure" of the width of the distribution) and σ is the standard deviation. Standard deviation is a widely used measure of variability. It shows how much variation or "dispersion" there is from the average. A low standard deviation indicates that the data points tend to be very close to the mean, whereas high standard deviation indicates that the data points are spread out over a large range of values. For distributions that have long tails, an alternative way to describe this variation is the FWHM, that is the width across the profile when it drops to half of its peak, or maximum, value (shown in Fig. A.12): the parameter σ for these distributions do not describe the core of the distribution well. Infact, the relationship between FWHM and the standard deviation for a gaussian profile σ is:

$$FWHM = 2\sqrt{2ln2}\sigma = 2,355\sigma. \tag{A.19}$$

FWHM is the most important measure for quantifying image sharpness.

The spectral and spatial bandwidths we have discussed, are defined as the widths of the band of light at Full Width Half Maximum.

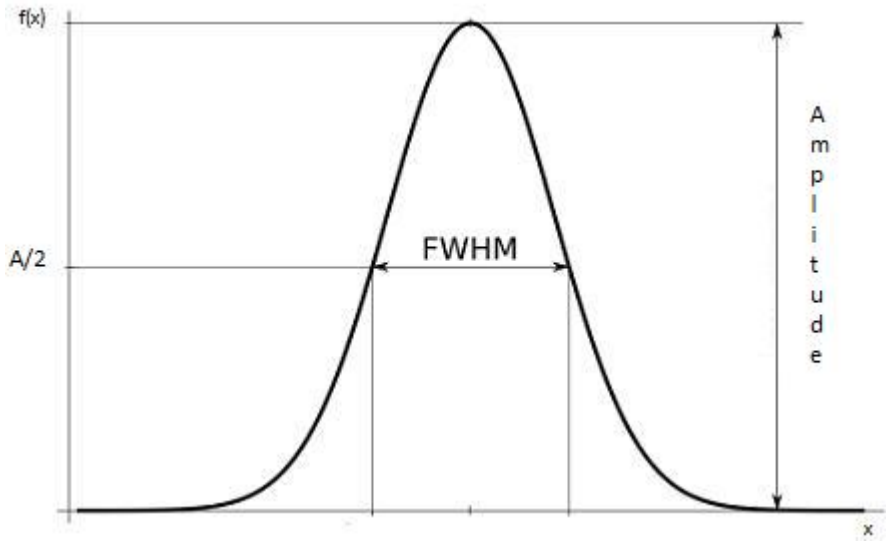

Figure A.12: Gaussian Profile and FWHM.

Bibliography

[1] B. Fleck, V. Domingo, A. Poland (1995), *The SOHO Mission*, Kluwer Academic Publishers, London.

[2] L.Actron, E.Bruner, W. Brown, B. Fawcett, W.Schweizer, R. Speer (2008), *Rocket Spectrogram of a solar flare in the 10-100 angstrom region.*

[3] L. Poletto (2010), *Ottiche e Strumenti XUV.*

[4] L. Poletto, G. Tondello (2001), *Grazing-incidence telescope-spectrograph for space solar-imaging spectroscopy.*

[5] F. Frassetto, S. Corraggia, L. Poletto (2010), *Spectrograph for solar imaging in the XUV domain.*

[6] A. Egbert, B. Tkachenko, S. Becker, B. Chichkov (2004), *Compact electron-based EUV source for at-wavelength metrology.*

[7] S. Rolt (2010), *Aberration Theory.*

[8] B. Aschenbach (1985), *X-ray telescopes.*

[9] A. Franks (1977), *X-ray optics.*

[10] C. Palmer (2005), *Diffraction Grating Handbook*, Erwin Loewen Editor, New York.